

# Recovering Whole-Brain Causal Connectivity under Indirect Observation with Applications to Human EEG and fMRI

Sangyoob Bae<sup>1</sup> Miruna Oprescu<sup>2</sup> David Keetae Park<sup>3</sup> Shinjae Yoo<sup>3</sup> Jiook Cha<sup>1</sup>

## Abstract

Inferring directed connectivity from neuroimaging is an ill-posed inverse problem: recorded signals are distorted by hemodynamic filtering and volume conduction, which can mask true neural interactions. Many existing methods conflate these observation artifacts with genuine neural influence, risking spurious causal graphs driven by the measurement process. We introduce INCAMA (INDirect CAusal MAmbo), a latent-space causal discovery framework that explicitly accounts for measurement physics to separate neural dynamics from indirect observations. INCAMA integrates a physics-aware inversion module with a nonstationarity-driven, delay-sensitive causal discovery model based on selective state-space sequences. Leveraging nonstationary mechanism shifts as soft interventions, we establish identifiability of delayed causal structure from indirect measurements and a stability bound that quantifies how inversion error affects graph recovery. We validate INCAMA on large-scale biophysical simulations across EEG and fMRI, where it significantly outperforms standard pipelines. We further demonstrate zero-shot generalization to real-world fMRI from the Human Connectome Project: without domain-specific fine-tuning, INCAMA recovers canonical visuomotor pathways (e.g.,  $V1 \rightarrow V2$  and  $M1 \leftrightarrow S1$ ) consistent with established neuroanatomy, supporting its use for whole-brain causal inference.

## 1. Introduction

Estimating directed brain connectivity from neuroimaging is a central goal in systems neuroscience, as it offers a

<sup>1</sup>Interdisciplinary Program in Artificial Intelligence, Seoul National University, Seoul, South Korea <sup>2</sup>Computer Science at Cornell University, Ithaca, New York, US <sup>3</sup>Brookhaven National Laboratory, Upton, New York, US. Correspondence to: Jiook Cha <connectome@snu.ac.kr>, Shinjae Yoo <sjyoo@bnl.gov>.

Preprint. February 11, 2026.

mechanistic account of how activity propagates across distributed neural circuits and underlies cognition and dysfunction (Bullmore & Sporns, 2009; Park & Friston, 2013). However, neuroimaging provides only indirect observations of neural activity: functional magnetic resonance imaging (fMRI) signals are temporally filtered by hemodynamics and contaminated by physiological noise (Friston et al., 2003; Logothetis, 2008a), while Electroencephalogram (EEG) measurements are spatially mixed through volume conduction and source leakage (Schoffelen & Gross, 2009). As a result, statistical dependencies in the observed signals can deviate substantially from the true causal interactions among latent neural populations, fundamentally complicating causal identifiability and inference (Peters et al., 2017).

Most existing approaches to causal discovery from neuroimaging are constrained by a fundamental trade-off between biophysical realism and scalability. Biophysically grounded models such as Dynamic Causal Modeling (DCM) explicitly couple latent neural dynamics with a measurement model, but quickly become computationally prohibitive beyond small networks (Friston et al., 2003). Scalable variants such as regression-DCM improve runtime, yet rely on approximations that can bias estimates in large, recurrent systems (Frässle et al., 2021). At the other extreme, scalable time-series methods (e.g., Granger causality and Vector Autoregression [VAR]) and recent neural causal models can be applied at whole-brain scale; however, when fit directly in the observation space, they are highly sensitive to *indirect observation effects* such as hemodynamic filtering and volume conduction. As a result, measurement distortions can be erroneously attributed to neural interactions, leading to spurious causal structure (Granger, 1969; Lütkepohl, 2005; Tank et al., 2021).

We propose a causal discovery framework that treats directed connectivity as a latent neural property, rather than a pattern directly observable in neuroimaging data. The framework explicitly separates—and links—two subproblems that are often conflated: recovering latent neural dynamics under measurement physics, and inferring delayed directed interactions from those dynamics. It first applies physics-aware inversion to reconstruct latent neural trajectories from indirect observations, leveraging modality-specific priors (e.g.,

Deep Neural Source Imaging Framework (DeepSIF) for EEG (Sun et al., 2022) and hemodynamic response function (HRF) aware deconvolution with region-specific variability for fMRI (Friston et al., 2003; Handwerker et al., 2004)). It then performs directed, delay-aware causal discovery in the latent space using a selective state-space sequence model, which adaptively focuses on informative temporal segments and enables scalable long-context modeling and sparse structure extraction at whole-brain resolution (Gu & Dao, 2024). Crucially, the framework leverages nonstationarity as an intrinsic feature of brain dynamics—reflecting latent regime shifts or evolving data-generating mechanisms—and exploits it as informative variation for orienting causal structure, rather than treating it as a nuisance (Huang et al., 2019; Schölkopf et al., 2021; Peters et al., 2017). Our primary contributions are three-fold:

- We introduce **INdirect CAusal MAmbo (INCAMA)**, an end-to-end latent-space causal discovery framework that integrates physics-aware neural inversion with scalable causal graph inference for indirect neuroimaging data.
- We provide a **theoretical analysis** establishing identifiability of delayed causal structure from indirect measurements, together with a stability bound that characterizes how inversion error propagates to graph recovery.
- We validate INCAMA on **large-scale biophysical simulations** with known ground truth and demonstrate zero-shot transfer to real fMRI data without finetuning, despite substantial modality-specific measurement distortion.

Overall, INCAMA offers a scalable and theoretically grounded route to whole-brain causal connectivity.

## 2. Background and Related Work

We provide a brief overview of related work here, with a more detailed discussion in [Appendix A](#).

**Causal discovery from brain data.** Inferring directed connectivity from neuroimaging is fundamentally challenged by indirect measurements and modality-specific confounds. Biophysically grounded models such as Dynamic Causal Modeling (DCM) explicitly capture neural–measurement transformations (Friston et al., 2003), but scale poorly beyond small networks, while regression variants improve efficiency at the cost of biased estimates in recurrent systems (Frässle et al., 2021). In contrast, scalable time-series methods based on Granger causality and VAR (Granger, 1969; Lütkepohl, 2005) are computationally efficient but highly sensitive to hemodynamic distortion, source mixing, delays, and nonstationarity when applied directly to observed signals. Recent neural causal models increase representational flexibility (Tank et al., 2021), yet with-

out explicit measurement modeling they remain vulnerable to spurious structure induced by the observation process rather than latent neural causality (Shimizu et al., 2006; Pearl, 2009). While both CausalMamba (Bae & Cha, 2025) and INCAMA leverage state-space sequence models, the focus and assumptions are fundamentally different. CausalMamba assumes direct observations and stationary dynamics, whereas INCAMA explicitly addresses indirect and modality-specific measurement processes.

**Causal discovery with nonstationary dynamics.** Nonstationarity can facilitate causal discovery by treating distribution shifts across time or contexts as “soft interventions” under the Independent Causal Mechanisms (ICM) principle (Peters et al., 2017; Schölkopf et al., 2021). Huang et al. (2019) formalize this idea using identifiable nonlinear state-space and structural equation models, showing that time-varying mechanisms can render directed structure identifiable and improve forecasting. Related approaches exploit independent changes in conditional modules (e.g., CD-NOD and extensions) (Zhang et al., 2017; Huang et al., 2020), invariance across unknown environments or time segments (Pfister et al., 2019), or jointly learned regime-dependent graphs (Saggiomo et al., 2020; Gao et al., 2023). We build most directly on the formulation of Huang et al. (2019), as it naturally targets lagged causal structure from nonstationary dynamics and aligns well with modern state-space models; unlike our setting, however, existing methods typically assume *direct* observations of the causal variables.

**Inverse problems in EEG and fMRI.** Despite substantial progress on inverse problems in EEG and fMRI, most inversion methods are developed as standalone preprocessing steps, decoupled from downstream causal analysis. In EEG, source localization approaches such as MNE (Hämäläinen & Ilmoniemi, 1994), sLORETA (Pascual-Marqui, 2002), and neural methods including DeepSIF (Sun et al., 2022) remain affected by residual source leakage and model mismatch. For fMRI, HRF deconvolution methods, including blind deconvolution (Wu et al., 2013) and DCM-style modeling (Friston et al., 2003), are sensitive to identifiability issues and modeling assumptions. As a consequence, inversion errors can propagate to downstream causal discovery, leading to biased connectivity estimates in decoupled inversion–then–inference pipelines.

**State-space sequence models.** State-space models (SSMs) provide a foundational framework for dynamical modeling in neuroscience, underpinning approaches such as Dynamic Causal Modeling (DCM) (Friston et al., 2003; Valdes-Sosa et al., 2011) and latent dynamical causal formulations (Huang et al., 2019). Recent deep structured SSM layers, including HiPPO/S4 and their variants, enable linear-time long-context modeling (Gu et al., 2020; 2021; Smith et al., 2022). Mamba further extends this class by introduc-

ing input-dependent selectivity, allowing the model to focus computation on information-dense temporal segments (Gu & Dao, 2024). We build on these advances to develop a scalable state-space framework for neural causal inference from *indirect* measurements, where temporal variation in latent dynamics carries informative structure.

### 3. Problem Setting: Causal Discovery from Indirect Human Brain Measurements

Let  $\mathbf{z}_t \in \mathbb{R}^N$  denote latent ROI/source neural activity at time  $t \in \{1, \dots, T\}$ , and let  $\mathbf{x}_t \in \mathbb{R}^M$  denote observed measurements (sensor-space EEG or fMRI-derived signals).

#### 3.1. Latent Delayed Dynamical SCM

We represent directed delayed interactions by a delayed graph  $\mathcal{G} = (V, E, \tau)$  with  $V = \{1, \dots, N\}$ , directed edges  $E \subseteq V \times V$ , and per-edge delays  $\tau_{ij} \in \{1, \dots, D\}$  for  $(i \rightarrow j) \in E$ . Define the parent set  $\text{Pa}(j) = \{i : (i \rightarrow j) \in E\}$ . The latent process follows a (possibly nonlinear) delayed dynamical SCM:

$$z_{j,t} = f_{j,t}(\{z_{i,t-\tau_{ij}} : i \in \text{Pa}(j)\}, \mathbf{u}_t) + \eta_{j,t}, \quad j \in V,$$

where  $\mathbf{u}_t$  denotes optional exogenous inputs (e.g., stimuli; set  $\mathbf{u}_t \equiv 0$  in resting-state), and  $\eta_{j,t}$  are exogenous disturbances. We allow nonstationarity through time-varying mechanisms  $f_{j,t}$  (equivalently,  $f_{j,t} = f_j(\cdot; \theta_j^{e(t)})$ ) with a latent environment index  $e(t)$ , consistent with the view that brain dynamics drift over time and conditions.

#### 3.2. Indirect Observation Model

Observed signals arise from a modality-specific forward operator with (possibly) finite memory:

$$\mathbf{x}_t = \mathcal{H}_\psi(\mathbf{z}_{t-L:t}) + \epsilon_t, \quad (1)$$

where  $\mathbf{z}_{t-L:t} := (\mathbf{z}_{t-L}, \mathbf{z}_{t-L+1}, \dots, \mathbf{z}_t)$  is a length- $(L+1)$  latent history block,  $L \geq 0$  is the observation memory length,  $\epsilon_t$  is measurement noise, and  $\psi$  corresponds to nuisance measurement parameters.

**fMRI (temporal distortion).** A common special case is HRF convolution,  $\mathbf{x}_t \approx \sum_{\ell=0}^L h_{\psi,\ell} \mathbf{z}_{t-\ell} + \epsilon_t$ , where  $h_\psi$  is an HRF parameterized by  $\psi$  (e.g., latency/dispersion/amplitude; possibly ROI-/subject-specific).

**EEG (spatial mixing).** A common approximation is instantaneous leadfield mixing,  $\mathbf{x}_t \approx \mathbf{L}_\psi \mathbf{z}_t + \epsilon_t$ , which corresponds to (1) with  $L = 0$ .  $\mathbf{L}_\psi$  depends on nuisances such as head model, electrode geometry, and referencing/montage.

Crucially, recovering  $\mathbf{z}_t$  from  $\mathbf{x}_t$  constitutes a classic ill-posed inverse problem, as  $\mathcal{H}_\psi$  is often non-invertible or under-determined without additional structure (e.g., biophysical priors, regularization, or parametric constraints).

This motivates an explicit physics-aware inversion stage and underlies our error-propagation analysis.

#### 3.3. Estimand and Learning Objective

Our causal estimand is the delayed directed graph  $\mathcal{G} = (V, E, \tau)$ . Given  $\mathbf{x}_{1:T}$ , our objective is to learn a map

$$\Phi : \mathbf{x}_{1:T} \mapsto (\widehat{\mathbf{z}}_{1:T}, \widehat{\mathcal{G}}), \quad (2)$$

that simultaneously: (i) solves a *regularized* inverse problem to recover latent trajectories  $\widehat{\mathbf{z}}_{1:T}$  (approximating  $\mathcal{H}_\psi^{-1}$  under biophysical constraints), and (ii) infers a sparse directed graph and interaction delays in latent space by exploiting the nonstationary structure of the recovered latent dynamics.

### 4. Identifiability under Indirect Observation and Nonstationarity

Our goal is to recover the delayed directed causal graph  $\mathcal{G} = (V, E, \tau)$  governing latent neural dynamics  $\mathbf{z}_{1:T}$  from indirect observations  $\mathbf{x}_t = \mathcal{H}_\psi(\mathbf{z}_{t-L:t}) + \epsilon_t$ . We call  $(E, \tau)$  *identifiable from the observed data* if it is uniquely determined (within our model class) by the distribution of  $\mathbf{x}_{1:T}$ .

Two obstacles arise: (i)  $\mathcal{H}_\psi$  is typically non-invertible or ill-conditioned in EEG/fMRI, and (ii) even with access to  $\mathbf{z}_{1:T}$ , causal direction may be ambiguous under stationarity. We therefore decompose identifiability into (a) *recoverability of the inverse problem* via (regularized) physics-aware inversion, and (b) *latent-space identifiability* enabled by nonstationary mechanism shifts, interpretable as “soft interventions” (ICM; Peters et al. (2017); Huang et al. (2019)).

In this section, we state assumptions for inversion recoverability and latent identifiability, then give identifiability and error-propagation results (proofs in [Appendix B](#)).

#### 4.1. Assumptions

We state assumptions in two groups. Assumptions [Assumption 4.1–Assumption 4.2](#) are standard for dynamical SCMs (Pearl, 2009; Peters et al., 2017). Assumptions [Assumption 4.3–Assumption 4.5](#) encode the two sources of identifiability we exploit: nonstationarity and recoverable inversion.

**Assumption 4.1** (No instantaneous effects (delayed feedback)). All directed interactions have strictly positive delay:  $\tau_{ij} \geq 1$  for all  $(i \rightarrow j) \in E$ .

**Assumption 4.2** (Latent causal sufficiency). The exogenous noises  $\{\eta_{j,t}\}_{j \in V}$  are jointly independent across  $j$  (conditional on the past), so there are no unmodeled latent confounders among the latent ROIs/sources represented by  $\mathbf{z}_t$ .

**Assumption 4.1** excludes instantaneous interactions by requiring strictly positive delays, so causal effects propagate forward in time and the time-unrolled graph is acyclic even

with feedback loops. **Assumption 4.2** is the standard “no hidden confounding among modeled variables” assumption required to interpret directed edges as direct causal effects.

**Assumption 4.3** (Nonstationary mechanisms as soft interventions). There exists an environment index  $e(t) \in \{1, \dots, E\}$  such that  $f_{j,t}(\cdot) = f_j(\cdot; \theta_j^{e(t)})$ . Moreover, the mechanism shifts  $\{\theta_j^e\}_e$  vary independently across modules  $j$  (ICM) and are sufficiently informative (non-degenerate) to distinguish candidate graphs within the model class.

**Assumption 4.3** formalizes the idea that drifts in effective connectivity, noise, or excitability act like “natural” interventions. Empirically, our simulator induces such drifts, and real recordings also exhibit nonstationary regime changes.

**Assumption 4.4** (Recoverable latent state under indirect observation). There exists a (regularized) inversion procedure  $g$  such that  $\hat{\mathbf{z}}_{1:T} = g(\mathbf{x}_{1:T})$  and

$$\frac{1}{T} \sum_{t=1}^T \|\hat{\mathbf{z}}_t - \mathbf{z}_t\|_2^2 \xrightarrow{T \rightarrow \infty} 0 \quad (\text{in probability}), \quad (3)$$

under the measurement model, up to known equivalences (e.g., per-node scaling conventions).

**Assumption 4.5** (Latent identifiability via Huang et al. (2019)). Assume the latent process  $\mathbf{z}_{1:T}$  lies in the identifiable nonstationary SEM/SSM class of Huang et al. (2019), adapted to our delayed-parent setting (i.e., parents of  $z_{j,t}$  may include  $\{z_{i,t-\tau_{ij}}\}$  with  $\tau_{ij} \in \{1, \dots, D\}$ ), and that **Assumption 4.3** holds. Then, within this model class, the delayed graph  $\mathcal{G} = (V, E, \tau)$  is identifiable from the joint distribution of  $\mathbf{z}_{1:T}$  (as  $T \rightarrow \infty$ ).

## 4.2. Main Results (proofs deferred)

Under **Assumption 4.5**, the delayed graph is identifiable from  $P(\mathbf{z}_{1:T})$  by Huang et al. (2019) (with the above delayed-parent adaptation). Our novel contributions are: (i) a reduction showing that consistent inversion (**Assumption 4.4**) transfers this guarantee to indirect observations  $\mathbf{x}_{1:T}$ , and (ii) an error bound quantifying how inversion error impacts downstream graph recovery.

**Theorem 4.6** (Identifiability from indirect observations via inversion). *Consider the model class where (i)  $\mathbf{z}_{1:T}$  is generated by a delayed dynamical SCM satisfying **Assumption 4.1–Assumption 4.5**, and (ii) observations follow  $\mathbf{x}_t = \mathcal{H}_\psi(\mathbf{z}_{t-L:t}) + \epsilon_t$  for which **Assumption 4.4** holds. Then the delayed graph  $\mathcal{G} = (V, E, \tau)$  is identifiable from the distribution of  $\mathbf{x}_{1:T}$  (as  $T \rightarrow \infty$ ), up to the known equivalences in **Assumption 4.4**.*

**Theorem 4.6** shows that consistent inversion transfers latent-space identifiability to indirect observations. Next, we quantify how inversion error propagates to graph estimation error.

**Continuous score representation (and top- $k$  sparsification).** We estimate a continuous score object (e.g.,  $S \in \mathbb{R}^{|V| \times |V|}$ , with optional delay scores) and interpret it as a weighted directed graph. In practice, we obtain a sparse edge set by selecting the top- $k$  largest-magnitude entries of the score matrix; we treat this as a post-processing step and defer its formal stability conditions to [Appendix B](#).

**Proposition 4.7** (Inversion error propagation). *Let  $\hat{\mathbf{z}}_{1:T} = g(\mathbf{x}_{1:T})$  and  $\hat{S} = h(\hat{\mathbf{z}}_{1:T})$ , where  $h$  is a continuous score function. Let  $S^*$  denote the score representation of the true delayed graph  $\mathcal{G}$ , and let  $\mathcal{L}$  be a loss on score objects. Define the distance  $d_T(\mathbf{z}, \mathbf{z}') := (\frac{1}{T} \sum_{t=1}^T \|\mathbf{z}_t - \mathbf{z}'_t\|_2^2)^{1/2}$ . Assume  $h$  is  $L$ -Lipschitz w.r.t.  $d_T$  and  $\mathcal{L}$ :*

$$\mathcal{L}(h(\mathbf{z}), h(\mathbf{z}')) \leq L d_T(\mathbf{z}, \mathbf{z}') \quad \forall \mathbf{z}, \mathbf{z}'.$$

Then

$$\begin{aligned} \mathbb{E}[\mathcal{L}(\hat{S}, S^*)] &\leq \mathbb{E}[\mathcal{L}(h(\mathbf{z}_{1:T}), S^*)] \\ &\quad + L \left( \mathbb{E} \left[ \frac{1}{T} \sum_{t=1}^T \|\hat{\mathbf{z}}_t - \mathbf{z}_t\|_2^2 \right] \right)^{1/2}. \end{aligned} \quad (4)$$

In [Proposition 4.7](#), the first term is the intrinsic error of the latent graph estimator (even with true  $\mathbf{z}$ ); the second term quantifies how inversion error degrades graph recovery.

**Corollary 4.8** (Consistency of the end-to-end estimator). *Assume **Assumption 4.4** and that, given access to  $\mathbf{z}_{1:T}$ , the score estimator  $h$  is consistent under the latent model class in **Assumption 4.5**:  $\mathcal{L}(h(\mathbf{z}), S^*) \xrightarrow{T \rightarrow \infty} 0$  in probability.*

*Then the end-to-end estimator  $\hat{S} = h(g(\mathbf{x}))$  is consistent, i.e.  $\mathcal{L}(\hat{S}, S^*) \xrightarrow{T \rightarrow \infty} 0$ .*

**Takeaway.** Nonstationary mechanism shifts yield latent-space identifiability (via Huang et al. (2019)); if the latent trajectories are consistently recoverable from indirect measurements, the delayed graph is identifiable from observed EEG/fMRI, with stability controlled by the inversion error bound in [Proposition 4.7](#).

## 5. INCAMA: Indirect Causal Mamba

We introduce **INCAMA** (Algorithm 1, Figure 1), a framework for learning directed causal connectivity from indirectly observed neuroimaging data by jointly modeling physics-aware inversion and latent-space causal discovery. Specifically, INCAMA reconstructs latent neural activity from distorted observations and infers directed interactions among the recovered latent variables in an end-to-end manner. Algorithmic details are provided in [Appendix C](#).

Formally, INCAMA learns an inference map

$$\Phi : x_{1:T} \mapsto (\hat{\mathbf{z}}_{1:T}, \hat{G}), \quad (5)$$

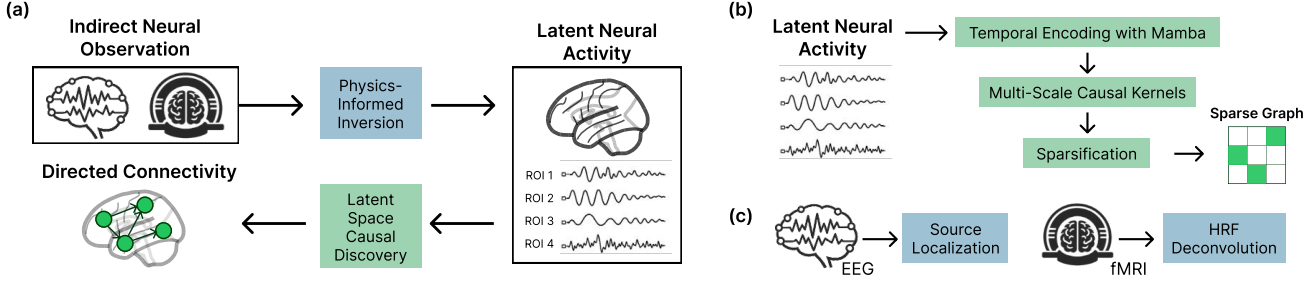


**Figure 1. Overview of INCAMA.** (a) **End-to-end framework.** INCAMA decomposes causal discovery from indirect neuroimaging measurements into physics-aware inversion and latent-space causal inference, mapping observed fMRI and EEG signals to latent neural dynamics before estimating directed connectivity. (b) **Latent-space causal discovery.** Directed, delay-aware causal inference is performed on latent neural trajectories using a scalable state-space sequence model with Mamba-based temporal encoding, yielding sparse and interpretable whole-brain connectivity. (c) **physics-aware inversion.** Modality-specific inversion modules, including HRF deconvolution for fMRI and source localization for EEG, recover latent neural activity from indirect and spatially mixed observations.

### Algorithm 1 Overview of INCAMA

**Require:** Observations  $x_{1:T}$  (EEG or fMRI)  
**Ensure:** Latent dynamics  $\hat{z}_{1:T}$  and causal graph  $\hat{G}$

- 1: **Stage 1: Physics-aware inversion**
- 2:  $\hat{z}_{1:T} \leftarrow g_\theta(x_{1:T})$
- 3: **Stage 2: Latent causal discovery**
- 4:  $h_{i,1:T} \leftarrow \text{Mamba}(\hat{z}_{i,1:T})$
- 5: Estimate delay-aware interactions and sparsify
- 6: **return**  $(\hat{z}_{1:T}, \hat{G})$

where  $x_{1:T}$  denotes observed EEG or fMRI signals,  $\hat{z}_{1:T}$  the reconstructed latent neural dynamics, and  $\hat{G}$  the directed causal graph. We follow the notation of Sections 3–4.

### 5.1. Physics-aware Inversion

Neuroimaging measurements provide only indirect observations of latent neural activity  $z_t$ , generated through a known but non-invertible forward process

$$x_t = H_\psi(z_{t-L:t}) + \varepsilon_t, \quad (6)$$

rendering recovery of  $z_{1:T}$  from  $x_{1:T}$  an ill-posed inverse problem. To address this, we learn a parameterized inverse model  $\hat{z}_{1:T} = g_\theta(x_{1:T})$ , whose architecture and training objectives are constrained by the known forward operator  $H_\psi$ , ensuring that the recovered trajectories correspond to physically meaningful neural activity rather than generic latent embeddings.

**Case 1: Spatial inversion in EEG.** EEG measurements are approximately instantaneous linear mixtures of neural sources (Baillet et al., 2001; Mosher et al., 1999),

$$x_t \approx L_\psi z_t + \varepsilon_t, \quad (7)$$

where  $L_\psi \in \mathbb{R}^{M \times R}$  is the leadfield matrix. We learn an inverse model  $\hat{z}_{1:T} = g_\theta^{\text{EEG}}(x_{1:T})$  constrained such that  $L_\psi \hat{z}_t$  reconstructs  $x_t$ , promoting causal discovery on spatially unmixed latent neural activity.

**Case 2: Temporal inversion in fMRI.** fMRI measurements are temporally blurred by the hemodynamic response function (HRF) (Friston et al., 2003; Logothetis, 2008b),

$$x_t \approx \sum_{\ell=0}^L h_{\psi,\ell} z_{t-\ell} + \varepsilon_t. \quad (8)$$

The inverse model jointly estimates latent neural activity and HRF parameters,  $(\hat{z}_{1:T}, \hat{h}_\psi) = g_\theta^{\text{fMRI}}(x_{1:T})$ , such that convolving  $\hat{z}_{1:T}$  with  $\hat{h}_\psi$  reconstructs the observed BOLD signal. Allowing region-specific HRFs mitigates hemodynamically induced temporal confounds (Handwerker et al., 2004; Deshpande et al., 2010; Rangaprakash et al., 2023).

### 5.2. Latent-Space Causal Discovery

Given reconstructed neural activity, the second stage estimates the directed, delay-aware causal graph  $\hat{G}$  governing the latent dynamics.

**Temporal encoding.** Each ROI time series  $\hat{z}_{i,1:T}$  is processed by a shared selective state-space sequence model,

$$h_{i,1:T} = \text{MAMBA}(\hat{z}_{i,1:T}), \quad (9)$$

which enables scalable long-context modeling of nonstationary temporal dependencies while sharing statistical structure across ROIs (Gu & Dao, 2024).

**Delay-aware and multi-scale interaction modeling.** Directed interactions are parameterized using a multi-lag linearized dynamics model,

$$\hat{z}_{t+1} = \sum_{\ell=1}^D A_\ell \hat{z}_{t-\ell} + \xi_t, \quad (10)$$

where  $A_\ell \in \mathbb{R}^{R \times R}$  captures causal influence at delay  $\ell$ . To reflect heterogeneous temporal scales in neural interactions due to synaptic delays, axonal conduction, and indirect

pathway transmission, delays are grouped into short-, mid-, and long-range regimes,

$$\hat{z}_{t+1} = \sum_{g \in \mathcal{G}} \sum_{\ell \in \mathcal{L}_g} A_{\ell}^{(g)} \hat{z}_{t-\ell} + \xi_t, \quad (11)$$

with  $\mathcal{G} = \{\text{short, mid, long}\}$ . Causal strength is obtained by aggregating kernel magnitudes across delays and temporal scales.

**Sparse graph extraction.** Assuming sparse brain connectivity, INCAMA retains only the top- $k$  entries of the aggregated causal strength matrix, yielding an interpretable directed graph.

### 5.3. Training Objective and End-to-End Optimization

Training is performed on simulated data with known ground-truth adjacency  $A^*$ . The total loss combines graph reconstruction, antisymmetry, and stability terms,

$$\mathcal{L}_{\text{total}} = \mathcal{L}_{\text{graph}} + \lambda_{\text{asym}} \mathcal{L}_{\text{asym}} + \lambda_{\text{stab}} \mathcal{L}_{\text{stab}}. \quad (12)$$

The model is trained end-to-end,

$$\min_{\theta} \mathbb{E} \left[ \mathcal{L}_{\text{total}}(\hat{A}(g_{\theta}(x_{1:T})), A^*) \right], \quad (13)$$

allowing gradients from the causal objective to shape the inverse model. Implementation details are provided in Appendix D.

**Transfer to real data.** After pretraining on biophysical simulations, the learned inference map  $\Phi$  is applied zero-shot to real fMRI data without finetuning (Section 6.3).

## 6. Experiments

### 6.1. Experimental Setup

**Simulated data.** We evaluate INCAMA on large-scale physics-aware simulations inspired by The Virtual Brain (TVB) (Sanz Leon et al., 2013), which generates whole-brain neural activity with known directed connectivity, transmission delays, and controlled nonstationarity. Realistic EEG and fMRI observations are obtained via biophysically grounded forward models. Simulation details are provided in Appendix F and Appendix G for EEG and fMRI, respectively.

**Real data.** For real-world validation, we use motor-task fMRI data from the Human Connectome Project (HCP S1200), parcellated into 68 cortical regions using the Desikan–Killiany atlas (Desikan et al., 2006). All models are trained exclusively on simulated data and transferred zero-shot to HCP data, where evaluation focuses on the consistency of inferred causal pathways with established motor network organization.

**Baselines.** We compare INCAMA against standard two-stage pipelines that combine signal inversion or deconvolution with linear or neural causal discovery. For EEG, baselines include classical source localization methods (MNE (Hämäläinen & Ilmoniemi, 1994), sLORETA (Pascual-Marqui, 2002), DeepSIF (Sun et al., 2022)) paired with Granger causality (Granger, 1969) or VAR (Lütkepohl, 2005), as well as neural baselines based on temporal convolutional networks (TCNs) (Bai et al., 2018) and graph neural networks (GNNs) (Kipf & Welling, 2017). For fMRI, we evaluate HRF deconvolution methods (FIR and Wiener) (Glover, 1999) combined with Granger causality or VAR, together with recent neural causal models such as TCDF (Nadéau & Bengio, 2018) and CNN-based estimators. Complete baseline definitions and hyperparameters are provided in Appendix H.

**Evaluation metrics.** Causal recovery is evaluated using F1 score, normalized Structural Hamming Distance (SHD) and Direction-aware Structural Hamming Distance (dSHD). All metrics are computed against ground-truth graphs for simulated data; formal definitions are provided in Appendix I.

### 6.2. Results on Simulated Data and Ablation Analysis

**EEG.** Table 1 reports causal recovery performance on simulated EEG data. Classical pipelines that combine source localization with linear causal models perform near chance, reflecting the strong impact of residual volume conduction and source leakage. Neural baselines offer modest improvements but remain limited under realistic sensor mixing. In contrast, INCAMA substantially improves F1, SHD, and dSHD, demonstrating effective recovery of latent causal structure despite indirect and spatially mixed observations.

Ablation results further clarify the source of these gains. Removing modality-specific inversion (i.e., omitting source localization) leads to a pronounced degradation in graph recovery, indicating that causal inference on mixed sensor signals remains unreliable even with expressive sequence models. Beyond inversion, exploiting time-varying latent dynamics consistently improves recovery compared to variants that assume time-invariant mechanisms. This supports the view that nonstationary changes in underlying neural processes provide informative variation for orienting directed and delayed causal relationships. Notably, the gains from temporal variation are more pronounced in EEG, consistent with its high temporal resolution (250 Hz), which preserves temporal delays and regime-dependent dynamics in the latent space.

**fMRI.** Table 2 summarizes results on simulated fMRI data. Classical HRF deconvolution combined with linear causal estimation remains strongly affected by hemodynamic confounds, including HRF mismatch and temporal blurring, and neural baselines show only limited improvement. IN-

Method	F1 $\uparrow$	SHD $\downarrow$	dSHD $\downarrow$
MNE + Granger	0.163 $\pm$ 0.000	0.530 $\pm$ 0.000	0.278 $\pm$ 0.000
MNE + VAR	0.160 $\pm$ 0.002	0.533 $\pm$ 0.002	0.280 $\pm$ 0.001
sLORETA + Granger	0.163 $\pm$ 0.000	0.530 $\pm$ 0.000	0.278 $\pm$ 0.000
sLORETA + VAR	0.162 $\pm$ 0.003	0.531 $\pm$ 0.003	0.279 $\pm$ 0.002
DeepSIF + Granger	0.176 $\pm$ 0.001	0.533 $\pm$ 0.001	0.279 $\pm$ 0.000
DeepSIF + TCN + sparse MLP	0.215 $\pm$ 0.000	0.495 $\pm$ 0.000	0.254 $\pm$ 0.000
sLORETA + TCN + sparse MLP	0.174 $\pm$ 0.003	0.534 $\pm$ 0.002	0.280 $\pm$ 0.001
DeepSIF + GNN + sparse MLP	0.192 $\pm$ 0.000	0.511 $\pm$ 0.001	0.265 $\pm$ 0.000
sLORETA + GNN + sparse MLP	0.193 $\pm$ 0.001	0.509 $\pm$ 0.001	0.264 $\pm$ 0.001
INCAMA (without source localization)	0.000 $\pm$ 0.000	0.102 $\pm$ 0.000	0.075 $\pm$ 0.000
INCAMA (Stationary data)	0.252 $\pm$ 0.034	0.148 $\pm$ 0.004	0.163 $\pm$ 0.002
<b>INCAMA (Nonstationary data)</b>	<b>0.643<math>\pm</math>0.012</b>	<b>0.081<math>\pm</math>0.010</b>	<b>0.109<math>\pm</math>0.009</b>

**Table 1. Causal discovery performance on TVB-simulated EEG data.** Under nonstationary dynamics, scalar error metrics (e.g., MAE) become ill-defined; we therefore report structure- and causality-aware metrics (F1, SHD, dSHD). For degenerate predictions with no recovered edges ( $F1 \approx 0$ ), SHD/dSHD can appear artificially low; we interpret such cases as failure to recover causal structure. Standard source localization (MNE, sLORETA) leaves redSHDual mixing that confuses linear causal models, whereas INCAMA effectively recovers true directed connectivity.

Method	F1 $\uparrow$	SHD $\downarrow$	dSHD $\downarrow$
FIR + Granger	0.247 $\pm$ 0.000	0.400 $\pm$ 0.000	0.384 $\pm$ 0.001
FIR + VAR	0.259 $\pm$ 0.000	0.450 $\pm$ 0.000	0.460 $\pm$ 0.000
Wiener + Granger	0.229 $\pm$ 0.000	0.352 $\pm$ 0.000	0.350 $\pm$ 0.001
Wiener + VAR	0.257 $\pm$ 0.000	0.450 $\pm$ 0.000	0.430 $\pm$ 0.000
rDCM	0.258 $\pm$ 0.006	0.450 $\pm$ 0.003	0.460 $\pm$ 0.003
Deconv + TCDF	0.000 $\pm$ 0.000	0.174 $\pm$ 0.001	0.177 $\pm$ 0.001
EndtoEndCNN	0.061 $\pm$ 0.073	0.534 $\pm$ 0.022	0.454 $\pm$ 0.002
INCAMA (without HRF deconvolution)	0.583 $\pm$ 0.006	0.093 $\pm$ 0.002	0.093 $\pm$ 0.002
INCAMA (Stationary data)	0.608 $\pm$ 0.001	0.089 $\pm$ 0.000	0.093 $\pm$ 0.000
<b>INCAMA (Nonstationary data)</b>	<b>0.610<math>\pm</math>0.005</b>	<b>0.088<math>\pm</math>0.001</b>	<b>0.092<math>\pm</math>0.001</b>

**Table 2. Causal discovery performance on TVB-simulated fMRI data.** Under nonstationary dynamics, scalar error metrics (e.g., MAE) are ill-defined; we therefore report structure- and causality-aware metrics (F1, SHD, dSHD).

Model	Right (RH)	Left (LH)
<b>INCAMA</b>	<b>0.667</b>	<b>0.833</b>
rDCM	0.152	0.129
Deconv+TCDF	0.000	0.000
EndtoEndCNN	0.147	0.153
FIR+VAR	0.144	0.131
FIR+GRANGER	0.127	0.160
WEINER+VAR	0.144	0.126
WEINER+GRANGER	0.110	0.109
Random Baseline	0.152	0.147

**Table 3. Causal pathway recovery rate (recall) on the HCP S1200 Motor Task.** Results are averaged across 1,078 subjects, evaluating how many canonical visuo-motor pathways are correctly recovered from real fMRI data.

CAMA achieves the best overall performance by jointly modeling HRF variability and delayed interactions within a shared latent space, enabling more accurate recovery of directed connectivity.

In contrast to EEG, stationary and nonstationary variants of INCAMA perform similarly in fMRI. This behavior is expected given the low sampling rate (0.5 Hz) and the strong temporal smoothing induced by the HRF, which attenuate effective temporal variation and limit the identifiability benefits of nonstationarity.

Across both modalities, classical two-stage pipelines—such as MNE/sLORETA followed by VAR or Granger causality in EEG, or FIR/Wiener HRF deconvolution followed by linear causal models in fMRI—share structural limitations under indirect observation. Linear lag-based models assume fixed-lag dependencies and are therefore highly sensitive to residual source mixing in EEG and temporal blurring in fMRI. Moreover, the strict separation of inversion and causal inference prevents downstream causal models from adapting to systematic errors introduced during inversion. By contrast, INCAMA couples inversion and causal discovery end-to-end in a shared latent space and leverages temporal

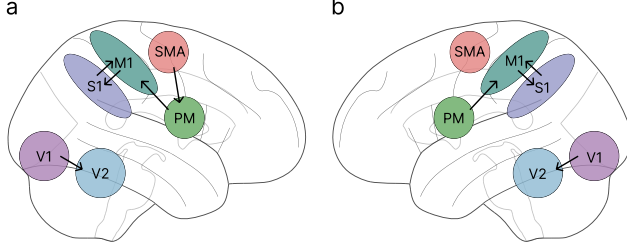


**Figure 2. Recovered average visuo-motor causal pathways in the (a) left and (b) right hemispheres.** Nodes correspond to standard neuroanatomical regions of interest (ROIs) defined by the Desikan–Killiany atlas. Arrows indicate the directional information flow inferred by INCAMA from real fMRI data of the HCP S1200 Motor Task, computed by averaging recovered causal graphs across 1,078 subjects. The resulting group-level structure reveals a consistent hierarchical progression from visual processing ( $V1 \rightarrow V2$ ), to motor planning ( $SMA \rightarrow PM$ ), and execution–feedback loops ( $M1 \leftrightarrow S1$ ).

structure in the recovered neural dynamics—particularly nonstationary variation—as informative signal for orienting directed, delayed causal relationships. Overall, these results support the central premise of INCAMA: accurate whole-brain causal inference requires explicitly accounting for both the observation process and the temporal structure of latent neural interactions.

### 6.3. Zero-shot Causal Inference on Real fMRI

We evaluate whether causal structure learned from simulation transfers to real data by applying INCAMA, without finetuning, to HCP S1200 motor-task fMRI.

**Canonical pathway recovery.** We focus on the visuo-motor pathway

$$V1 \rightarrow V2 \rightarrow SMA \rightarrow PM \rightarrow M1 \rightarrow S1 \rightarrow M1,$$

a well-established circuit activated during motor execution (Nassi & Callaway, 2007; Hoshi & Tanji, 2004). As shown in Fig. 2 and Table 3, INCAMA recovers a substantial fraction of canonical edges, consistently outperforming random and baseline methods. This indicate that causal representations learned under controlled biophysical simulations generalize meaningfully to real human brain data.

### 6.4. Computational Efficiency

We evaluate the trade-off between causal discovery performance (F1 score) and computational cost (GFLOPs) to assess the scalability of INCAMA. As shown in Table 4, INCAMA lies on the Pareto frontier, achieving a favorable balance between accuracy and efficiency compared to both biophysically grounded and lightweight neural baselines.

Biophysically grounded approaches such as regression-DCM (rDCM) scale poorly with network size, requiring  $\mathcal{O}(10^1)$  GFLOPs for whole-brain analysis while yielding

Method	Complexity	GFLOPs	$F1 \uparrow$
rDCM	$\mathcal{O}(I \times [T \times R^3 + R^4])$	$1.0 \times 10^1$	0.258
EndtoEndCNN	$\mathcal{O}(R \times T + R^2)$	$2.0 \times 10^{-5}$	0.061
Deconv+TCDF	$\mathcal{O}(R \times T + R^2)$	$3.5 \times 10^{-4}$	0.289
INCAMA	$\mathcal{O}(R \times T^2 + R^2 \times T)$	$5.0 \times 10^{-3}$	<b>0.610</b>

**Table 4. Computational complexity–accuracy trade-off in causal discovery.** Methods are evaluated on TVB-simulated fMRI with  $R = 68$  ROIs and  $T = 240$  timepoints. For rDCM, we use  $I = 100$  inference iterations. Inference cost denotes the per-subject computational complexity, accounting for both Stage 1 (physics-aware inversion) and Stage 2 (causal discovery). INCAMA achieves a three-order-of-magnitude reduction in FLOPs compared to rDCM, while attaining a  $2.4 \times$  higher F1 score, demonstrating Pareto-optimal performance.

low F1 scores (0.258) (Friston et al., 2003; Frässle et al., 2021). In contrast, neural baselines such as CNN (0.326) and Deconv+TCDF (0.289) incur negligible computational cost ( $< 10^{-4}$  GFLOPs) but fail to recover causal structure effectively (Bai et al., 2018).

INCAMA achieves substantially higher causal recovery ( $F1=0.610$ ) at low computational cost ( $5.0 \times 10^{-3}$  GFLOPs), enabled by the selective state-space mechanism of the Mamba architecture (Gu & Dao, 2024). These results position INCAMA as a scalable approach to whole-brain directed connectivity inference without sacrificing causal accuracy.

## 7. Conclusion

We introduced INCAMA, a physics-aware causal discovery framework for recovering directed whole-brain connectivity from indirect neuroimaging measurements. By explicitly separating measurement inversion from latent-space causal inference and treating temporal variation in neural dynamics as informative structure, INCAMA avoids conflating observation artifacts with genuine neural interactions. We established identifiability conditions and a stability bound that characterize when delayed causal graphs can be reliably recovered under indirect observation. Across large-scale simulations, INCAMA consistently outperforms biophysical and neural baselines while remaining computationally efficient, and generalizes zero-shot from simulation to real HCP motor-task fMRI, recovering canonical visuo-motor pathways. Overall, these results suggest that accurate whole-brain causal inference requires viewing directed connectivity as a latent neural property and jointly accounting for measurement physics and temporal structure, providing a general blueprint for causal discovery from indirect and distorted observations.

## 8. Impact Statement

This work aims to improve the reliability of directed connectivity estimates from neuroimaging by explicitly modeling measurement distortion (e.g., hemodynamics, source mixing) rather than attributing these effects to neural interactions. If successful, such tools could support scientific understanding of brain circuit organization and potentially inform hypothesis generation in clinical neuroscience. However, inferred causal graphs from observational neuroimaging remain sensitive to modeling assumptions, preprocessing choices, and unmodeled confounding, and should not be used in isolation to guide medical decisions. There are also privacy considerations when working with human neuroimaging data; our experiments use established de-identified datasets and we report only aggregate results.

## References

Bae, S. and Cha, J. Causalmamba: Scalable conditional state space models for neural causal inference. *arXiv preprint arXiv:2510.17318*, 2025.

Bai, S., Kolter, J. Z., and Koltun, V. An empirical evaluation of generic convolutional and recurrent networks for sequence modeling. *arXiv preprint arXiv:1803.01271*, 2018.

Baillet, S., Mosher, J. C., and Leahy, R. M. Electromagnetic brain mapping. *IEEE Signal Processing Magazine*, 2001.

Barnett, L. and Seth, A. K. The mvgc multivariate granger causality toolbox: a new approach to granger-causal inference. *Journal of neuroscience methods*, 223:50–68, 2014.

Bullmore, E. and Sporns, O. Complex brain networks: graph theoretical analysis of structural and functional systems. *Nature reviews neuroscience*, 10(3):186–198, 2009.

Dao, T. and Gu, A. Transformers are SSMs: Generalized models and efficient algorithms through structured state space duality. In *International Conference on Machine Learning*, volume 235 of *Proceedings of Machine Learning Research*. PMLR, 2024. URL <https://proceedings.mlr.press/v235/dao24a.html>.

Daunizeau, J., David, O., and Stephan, K. E. Dynamic causal modelling: a critical review of the biophysical and statistical foundations. *Neuroimage*, 58(2):312–322, 2011.

Deshpande, G., Sathian, K., and Hu, X. Effect of hemodynamic variability on Granger causality analysis of fMRI data. *NeuroImage*, 2010.

Desikan, R. S. et al. An automated labeling system for subdividing the human cerebral cortex on mri scans. *NeuroImage*, 31(3):968–980, 2006.

Frässle, S., Harrison, S. J., Heinze, J., Clementz, B. A., Tamminga, C. A., Sweeney, J. A., Gershon, E. S., Kesavan, M. S., Pearlson, G. D., Powers, A., et al. Regression dynamic causal modeling for resting-state fmri. *Human brain mapping*, 42(7):2159–2180, 2021.

Friston, K. J., Harrison, L., and Penny, W. Dynamic causal modelling. *Neuroimage*, 19(4):1273–1302, 2003.

Gao, S., Addanki, R., Yu, T., Rossi, R., and Kocaoglu, M. Causal discovery in semi-stationary time series. *Advances in Neural Information Processing Systems*, 36:46624–46657, 2023.

Glover, G. H. Deconvolution of impulse response in event-related bold fmri1. *Neuroimage*, 9(4):416–429, 1999.

Goel, K., Gu, A., Donahue, C., and Ré, C. It’s raw! audio generation with state-space models. In *International conference on machine learning*, pp. 7616–7633. PMLR, 2022.

Granger, C. W. Investigating causal relations by econometric models and cross-spectral methods. *Econometrica: journal of the Econometric Society*, pp. 424–438, 1969.

Gu, A. and Dao, T. Mamba: Linear-time sequence modeling with selective state spaces. In *First conference on language modeling*, 2024.

Gu, A., Dao, T., Ermon, S., Rudra, A., and Ré, C. Hippo: Recurrent memory with optimal polynomial projections. *Advances in neural information processing systems*, 33: 1474–1487, 2020.

Gu, A., Goel, K., and Ré, C. Efficiently modeling long sequences with structured state spaces. *arXiv preprint arXiv:2111.00396*, 2021.

Gu, A., Goel, K., Gupta, A., and Ré, C. On the parameterization and initialization of diagonal state space models. *Advances in Neural Information Processing Systems*, 35: 35971–35983, 2022a.

Gu, A., Goel, K., and Ré, C. Efficiently modeling long sequences with structured state spaces. In *International Conference on Learning Representations*, 2022b. doi: 10.48550/arXiv.2111.00396. URL <https://openreview.net/forum?id=uYLFozivlAC>.

Hämäläinen, M. S. and Ilmoniemi, R. J. Interpreting magnetic fields of the brain: minimum norm estimates. *Medical & Biological Engineering & Computing*, 32(1):35–42, 1994.

Handwerker, D. A., Ollinger, J. M., and D’Esposito, M. Variation of BOLD hemodynamic responses across subjects and brain regions and their effects on statistical analyses. *NeuroImage*, 21(4):1639–1651, 2004.

Hoshi, E. and Tanji, J. Differential roles of neuronal activity in the supplementary and presupplementary motor areas: from information retrieval to motor planning and execution. *Journal of neurophysiology*, 92(6):3482–3499, 2004.

Huang, B., Zhang, K., and Schölkopf, B. Identification of time-dependent causal model: A gaussian process treatment. In *IJCAI*, pp. 3561–3568, 2015.

Huang, B., Zhang, K., Gong, M., and Glymour, C. Causal discovery and forecasting in nonstationary environments with state-space models. In *International conference on machine learning*, pp. 2901–2910. Pmlr, 2019.

Huang, B., Zhang, K., Zhang, J., Ramsey, J., Sanchez-Romero, R., Glymour, C., and Schölkopf, B. Causal discovery from heterogeneous/nonstationary data. *Journal of Machine Learning Research*, 21(89):1–53, 2020.

Kipf, T. N. and Welling, M. Semi-supervised classification with graph convolutional networks. *ICLR*, 2017.

Logothetis, N. K. What we can do and what we cannot do with fmri. *Nature*, 453(7197):869–878, 2008a.

Logothetis, N. K. What we can do and what we cannot do with fmri. *Nature*, 453(7197):869–878, 2008b.

Lütkepohl, H. *New introduction to multiple time series analysis*. Springer, 2005.

Mosher, J. C., Leahy, R. M., and Lewis, P. S. Eeg and meg: Forward solutions for inverse methods. *IEEE Transactions on Biomedical Engineering*, 46(3):245–259, 1999.

Nadéau, C. and Bengio, Y. Temporal causal discovery framework. *NeurIPS*, 2018.

Nag, S. and Uludag, K. Transformer-aided dynamic causal model for scalable estimation of effective connectivity. *Imaging Neuroscience*, 2:1–22, 2024.

Nassi, J. J. and Callaway, E. M. Specialized circuits from primary visual cortex to v2 and area mt. *Neuron*, 55(5):799–808, 2007.

Pandarinath, C., O’Shea, D. J., Collins, J., Jozefowicz, R., Stavisky, S. D., Kao, J. C., Trautmann, E. M., Kaufman, M. T., Ryu, S. I., Hochberg, L. R., et al. Inferring single-trial neural population dynamics using sequential auto-encoders. *Nature methods*, 15(10):805–815, 2018.

Park, H.-J. and Friston, K. Structural and functional brain networks: from connections to cognition. *Science*, 342 (6158):1238411, 2013.

Pascual-Marqui, R. D. Standardized low-resolution brain electromagnetic tomography (sloreta): technical details. *Methods and Findings in Experimental and Clinical Pharmacology*, 24:5–12, 2002.

Pearl, J. *Causality*. Cambridge university press, 2009.

Peters, J., Janzing, D., and Schölkopf, B. *Elements of causal inference: foundations and learning algorithms*. The MIT press, 2017.

Pfister, N., Bühlmann, P., and Peters, J. Invariant causal prediction for sequential data. *Journal of the American Statistical Association*, 114(527):1264–1276, 2019.

Rangaprakash, D. et al. The confound of hemodynamic response function variability in human resting-state fMRI connectivity. *Frontiers in Neuroscience*, 2023.

Sadeghi, A., Gopal, A., and Fesanghary, M. Causal discovery from nonstationary time series. *International Journal of Data Science and Analytics*, 19(1):33–59, 2025.

Saggioro, E., de Wiljes, J., Kretschmer, M., and Runge, J. Reconstructing regime-dependent causal relationships from observational time series. *Chaos: An Interdisciplinary Journal of Nonlinear Science*, 30(11), 2020.

Sanz Leon, P., Knock, S. A., Woodman, M. M., Domide, L., Mersmann, J., McIntosh, A. R., and Jirsa, V. The virtual brain: a simulator of primate brain network dynamics. *Frontiers in neuroinformatics*, 7:10, 2013.

Schoffelen, J.-M. and Gross, J. Source connectivity analysis with meg and eeg. *Human brain mapping*, 30(6):1857–1865, 2009.

Schölkopf, B., Locatello, F., Bauer, S., Ke, N. R., Kalchbrenner, N., Goyal, A., and Bengio, Y. Toward causal representation learning. *Proceedings of the IEEE*, 109(5):612–634, 2021.

Shimizu, S., Hoyer, P. O., Hyvärinen, A., Kerminen, A., and Jordan, M. A linear non-gaussian acyclic model for causal discovery. *Journal of Machine Learning Research*, 7(10), 2006.

Smith, J. T., Warrington, A., and Linderman, S. W. Simplified state space layers for sequence modeling. *arXiv preprint arXiv:2208.04933*, 2022.

Smith, J. T. H., Warrington, A., and Linderman, S. W. Simplified state space layers for sequence modeling. In *International Conference on Learning Representations*, 2023. doi: 10.48550/arXiv.2208.04933. URL <https://openreview.net/forum?id=Ai8Hw3AXqks>.

Sun, R., Sohrabpour, A., Worrell, G. A., and He, B. Deep neural networks constrained by neural mass models improve electrophysiological source imaging of spatiotemporal brain dynamics. *Proceedings of the National Academy of Sciences*, 119(31):e2201128119, 2022.

Tank, A., Covert, I., Foti, N., Shojaie, A., and Fox, E. B. Neural granger causality. *IEEE Transactions on Pattern Analysis and Machine Intelligence*, 44(8):4267–4279, 2021.

Valdes-Sosa, P. A., Roebroeck, A., Daunizeau, J., and Friston, K. Effective connectivity: influence, causality and biophysical modeling. *Neuroimage*, 58(2):339–361, 2011.

Wu, G.-R., Liao, W., Stramaglia, S., Ding, J.-R., Chen, H., and Marinazzo, D. A blind deconvolution approach to recover effective connectivity brain networks from resting state fmri data. *Medical image analysis*, 17(3):365–374, 2013.

Yin, Z. and Barucca, P. Deep recurrent modelling of granger causality with latent confounding. *Expert Systems with Applications*, 207:118036, 2022.

Yu, B. M., Cunningham, J. P., Santhanam, G., Ryu, S., Shenoy, K. V., and Sahani, M. Gaussian-process factor analysis for low-dimensional single-trial analysis of neural population activity. *Advances in neural information processing systems*, 21, 2008.

Yu, Y., Chen, J., Gao, T., and Yu, M. Dag-gnn: Dag structure learning with graph neural networks. In *International conference on machine learning*, pp. 7154–7163. PMLR, 2019.

Zhang, K., Huang, B., Zhang, J., Glymour, C., and Schölkopf, B. Causal discovery from nonstationary/heterogeneous data: Skeleton estimation and orientation determination. In *IJCAI: Proceedings of the Conference*, volume 2017, pp. 1347, 2017.

Zheng, X., Aragam, B., Ravikumar, P. K., and Xing, E. P. Dags with no tears: Continuous optimization for structure learning. *Advances in neural information processing systems*, 31, 2018.

## A. Extended Literature Review

**Causal discovery from brain data.** Inferring directed interactions from neuroimaging data has long relied on frameworks such as Dynamic Causal Modeling (DCM) and Granger Causality (GC) (Friston et al., 2003; Granger, 1969). DCM explicitly incorporates biophysical mechanisms by modeling the mapping from latent neural activity to observed hemodynamic responses, but in practice its performance is highly sensitive to model assumptions (e.g., fixed or misspecified HRFs) and does not scale favorably to whole-brain settings (Daunizeau et al., 2011; Nag & Uludag, 2024). GC-based approaches, by contrast, operate directly on observed time series and are therefore vulnerable to hemodynamic distortions, capturing statistical dependencies that may diverge from underlying neural causation (Yin & Barucca, 2022; Barnett & Seth, 2014). More general causal structure learning methods, including NOTEARS (Zheng et al., 2018) and DAG-GNN (Yu et al., 2019), offer scalable optimization-based formulations but remain poorly matched to neuroimaging applications, as they do not explicitly address indirect measurement processes or region-specific neurovascular variability. The closest related work is CausalMamba (Bae & Cha, 2025), which applies Mamba-style sequence modeling to causal discovery. However, CausalMamba assumes stationary dynamics and indirect observations, and does not address causal identifiability under indirect and modality-specific measurement distortions. In contrast, INCAMA explicitly models indirect observation processes per modalities (e.g., hemodynamics and sensor mixing) via a physics-aware inversion stage, and enables regime-conditioned causal discovery beyond the stationary setting. Moreover, CausalMamba focuses on relatively small-scale graphs and does not consider multi-scale causal kernels or whole-brain inference, whereas INCAMA is designed for scalable, whole-brain causal recovery across modalities, including both fMRI and EEG.

**Causal discovery with nonstationary dynamics.** While many time-series causal discovery methods assume stationary mechanisms, real systems often exhibit distribution shifts over time or across contexts. A line of work shows that such nonstationarity can be exploited as informative variation—akin to a sequence of soft interventions—to improve identifiability of causal direction. Early time-dependent functional causal models treat time as an explicit variable and use Gaussian-process priors to estimate smoothly varying causal effects (Huang et al., 2015). The CD-NOD framework extends constraint-based discovery to heterogeneous/nonstationary data by detecting which conditional modules change and orienting edges via independent changes across modules (Zhang et al., 2017; Huang et al., 2020). Complementarily, Huang et al. model nonstationary time series with identifiable nonlinear state-space causal models with time-varying causal strengths and noise, linking causal discovery to improved forecasting (Huang et al., 2019). Related invariance-based approaches identify causal predictors in sequential settings by searching for conditional distributions that remain stable across unknown time segments/environments (Pfister et al., 2019). More recent methods address regime-dependent causal graphs by jointly inferring latent regimes and causal links (Saggiaro et al., 2020; Gao et al., 2023), and refine CD-NOD-style ideas to explicitly handle lagged nonstationary time series (Sadeghi et al., 2025). In this work, we adopt the perspective of Huang et al. (2019)—viewing nonstationarity as providing the mechanism shifts needed for identifiability in dynamical systems—because it aligns naturally with flexible state-space/sequence-model parameterizations; however, unlike our neuroimaging setting, most of this literature assumes *direct* access to the causal variables rather than indirect, physics-corrupted measurements.

**Limitations of inverse modeling in EEG and fMRI.** EEG source localization methods such as MNE (Hämäläinen & Ilmoniemi, 1994) and sLORETA (Pascual-Marqui, 2002) provide distributed inverse solutions but are known to suffer from depth bias, spatial smoothing, and source leakage, which can introduce spurious dependencies between reconstructed sources. Neural approaches such as DeepSIF (Sun et al., 2022) improve localization accuracy under realistic simulations but rely on training distributions and forward models that may not generalize across subjects, sensor configurations, or noise regimes. In fMRI, blind deconvolution (Wu et al., 2013) methods attempt to jointly estimate latent neural activity and hemodynamic responses from BOLD signals alone, but this joint estimation problem is weakly identifiable and often implemented via non-differentiable, multi-stage pipelines, limiting their integration with end-to-end learning. DCM-style HRF modeling (Friston et al., 2003) provides a biophysically interpretable alternative but requires strong structural and parametric assumptions and scales poorly to whole-brain settings. As a result, residual inversion mismatch remains unavoidable in practice and can propagate nontrivially to downstream causal discovery.

**State-space sequence models.** State-space models (SSMs) describe dynamical systems through latent state transitions coupled to an observation model, and form the basis of classical filtering/smoothing and system identification. In neuroscience, SSMs are central to effective-connectivity methods such as Dynamic Causal Modeling (DCM), which uses biophysically informed state and observation equations to connect latent neural dynamics to measured fMRI/EEG/MEG signals (Friston et al., 2003; Daunizeau et al., 2011; Valdes-Sosa et al., 2011); variants such as regression-DCM aim to improve scalability to larger networks (Frässle et al., 2021). SSM formulations also appear in data-driven latent dynamical models used to extract low-dimensional neural trajectories from high-dimensional recordings (e.g., GPFA and LFADS) (Yu et al., 2008;

Pandarinath et al., 2018). Beyond neuroscience, SSMs have been used directly for causal discovery in nonstationary time series, where time-varying parameters/mechanisms provide the variation needed for identifiability (Huang et al., 2019). In machine learning, a parallel line of “deep” structured SSM sequence models repurposes linear SSMs as scalable alternatives to attention: HiPPO introduces principled continuous-time memory operators (Gu et al., 2020), S4 provides an efficient parameterization for long-range sequence modeling (Gu et al., 2022b), and simplified variants such as S4D and S5 improve practicality while retaining long-context performance (Gu et al., 2022a; Smith et al., 2023). These layers can often be computed either via parallel scans or as recurrent updates, enabling long-sequence applications across modalities (e.g., SaShiMi for raw audio generation) (Goel et al., 2022). Mamba further introduces input-dependent selectivity and a hardware-aware “selective scan” to achieve strong performance on information-dense sequences with linear-time scaling (Gu & Dao, 2024), and subsequent work connects SSMs and masked attention through structured state-space duality (Mamba-2/SSD) (Dao & Gu, 2024). We leverage these advances by using a scalable SSM backbone for long neural recordings while preserving a biophysically interpretable separation between latent dynamics and measurement physics.

## B. Proofs for Section 4

We provide proofs for [Theorem 4.6](#), [Proposition 4.7](#), and [Corollary 4.8](#). Throughout, let  $\widehat{\mathbf{z}}_{1:T} = g(\mathbf{x}_{1:T})$  denote the (regularized) inversion output from [Assumption 4.4](#), and let  $\widehat{S} = h(\widehat{\mathbf{z}}_{1:T})$  denote the continuous score estimate in [Proposition 4.7](#). Let  $S^*$  denote the score representation of the true delayed graph  $\mathcal{G}$ . Let  $d_T$  be the trajectory distance  $d_T(\mathbf{z}, \mathbf{z}') := \left( \frac{1}{T} \sum_{t=1}^T \|\mathbf{z}_t - \mathbf{z}'_t\|_2^2 \right)^{1/2}$ . When [Assumption 4.4](#) holds “up to known equivalences” (e.g., per-node scalings), interpret  $d_T$  after applying the corresponding canonical alignment.

### B.1. A basic approximation lemma for path distributions

We treat the full latent trajectory as a single vector  $\mathbf{z}_{1:T} := (\mathbf{z}_1, \dots, \mathbf{z}_T) \in \mathbb{R}^{NT}$ , and measure trajectory error by the per-time RMS distance

$$d_T(\mathbf{z}, \mathbf{z}') := \left( \frac{1}{T} \sum_{t=1}^T \|\mathbf{z}_t - \mathbf{z}'_t\|_2^2 \right)^{1/2}.$$

This is the natural scale for our inversion assumption (3). The lemma below says that if the inversion error vanishes in this metric (in probability), then *any bounded, Lipschitz summary statistic of the entire path* has (asymptotically) the same expectation under the reconstructed path  $\widehat{\mathbf{z}}_{1:T}$  and the true path  $\mathbf{z}_{1:T}$ . Equivalently, the two path distributions become close in the bounded-Lipschitz (weak) sense.

Let  $\mathcal{BL}(1, 1)$  denote the class of functions  $\varphi : \mathbb{R}^{NT} \rightarrow \mathbb{R}$  such that: (i)  $|\varphi(\mathbf{z})| \leq 1$  for all  $\mathbf{z}$ , and (ii)  $\varphi$  is 1-Lipschitz w.r.t.  $d_T$ , i.e.,

$$|\varphi(\mathbf{z}) - \varphi(\mathbf{z}')| \leq d_T(\mathbf{z}, \mathbf{z}') \quad \forall \mathbf{z}, \mathbf{z}' \in \mathbb{R}^{NT}.$$

(Examples include many “smooth” path functionals, e.g., averages of bounded Lipschitz per-time features, or bounded versions of correlation/energy statistics; the Lipschitz condition encodes robustness to small reconstruction errors.)

**Lemma B.1** (Vanishing reconstruction error implies vanishing test-function gap). *If  $d_T(\widehat{\mathbf{z}}, \mathbf{z}) \xrightarrow[T \rightarrow \infty]{P} 0$ , then for every  $\varphi \in \mathcal{BL}(1, 1)$ ,*

$$\left| \mathbb{E}[\varphi(\widehat{\mathbf{z}}_{1:T})] - \mathbb{E}[\varphi(\mathbf{z}_{1:T})] \right| \xrightarrow[T \rightarrow \infty]{} 0.$$

*In particular, defining the bounded-Lipschitz distance between path laws*

$$d_{BL}(P(\widehat{\mathbf{z}}_{1:T}), P(\mathbf{z}_{1:T})) := \sup_{\varphi \in \mathcal{BL}(1, 1)} \left| \mathbb{E}[\varphi(\widehat{\mathbf{z}}_{1:T})] - \mathbb{E}[\varphi(\mathbf{z}_{1:T})] \right|,$$

*we have  $d_{BL}(P(\widehat{\mathbf{z}}_{1:T}), P(\mathbf{z}_{1:T})) \rightarrow 0$ .*

*Proof.* Fix any  $\varphi \in \mathcal{BL}(1, 1)$ . By the triangle inequality,

$$\left| \mathbb{E}[\varphi(\widehat{\mathbf{z}}_{1:T})] - \mathbb{E}[\varphi(\mathbf{z}_{1:T})] \right| \leq \mathbb{E} \left[ |\varphi(\widehat{\mathbf{z}}_{1:T}) - \varphi(\mathbf{z}_{1:T})| \right].$$

Now use (ii) (Lipschitzness) and (i) (boundedness): Lipschitzness gives  $|\varphi(\widehat{\mathbf{z}}_{1:T}) - \varphi(\mathbf{z}_{1:T})| \leq d_T(\widehat{\mathbf{z}}, \mathbf{z})$ , while boundedness implies the trivial bound  $|\varphi(\widehat{\mathbf{z}}_{1:T}) - \varphi(\mathbf{z}_{1:T})| \leq 2$ . Combining,

$$|\varphi(\widehat{\mathbf{z}}_{1:T}) - \varphi(\mathbf{z}_{1:T})| \leq \min\{2, d_T(\widehat{\mathbf{z}}, \mathbf{z})\}.$$

Therefore,

$$\left| \mathbb{E}[\varphi(\widehat{\mathbf{z}}_{1:T})] - \mathbb{E}[\varphi(\mathbf{z}_{1:T})] \right| \leq \mathbb{E}[\min\{2, d_T(\widehat{\mathbf{z}}, \mathbf{z})\}].$$

To show the RHS vanishes, fix  $\epsilon > 0$  and split on the event  $A_T := \{d_T(\widehat{\mathbf{z}}, \mathbf{z}) \leq \epsilon\}$ :

$$\begin{aligned} \mathbb{E}[\min\{2, d_T(\widehat{\mathbf{z}}, \mathbf{z})\}] &= \mathbb{E}[\min\{2, d_T(\widehat{\mathbf{z}}, \mathbf{z})\} \mathbf{1}_{A_T}] + \mathbb{E}[\min\{2, d_T(\widehat{\mathbf{z}}, \mathbf{z})\} \mathbf{1}_{A_T^c}] \\ &\leq \epsilon \cdot \mathbb{P}(A_T) + 2 \cdot \mathbb{P}(A_T^c) \leq \epsilon + 2 \mathbb{P}(d_T(\widehat{\mathbf{z}}, \mathbf{z}) > \epsilon). \end{aligned}$$

Since  $d_T(\widehat{\mathbf{z}}, \mathbf{z}) \rightarrow 0$  in probability, the probability term tends to 0 as  $T \rightarrow \infty$ , so the RHS tends to  $\epsilon$ . Because  $\epsilon > 0$  was arbitrary, the RHS (and hence the test-function gap) must converge to 0. The final claim about  $d_{BL}$  follows immediately by taking the supremum over  $\varphi \in \mathcal{BL}(1, 1)$ .  $\square$

**Remark (how we use the lemma).** Lemma B.1 justifies treating  $\widehat{\mathbf{z}}_{1:T}$  as an ‘‘asymptotically equivalent’’ surrogate for  $\mathbf{z}_{1:T}$  for any downstream procedure whose relevant statistics are continuous/robust in the  $d_T$  metric. In our setting, this enables a clean reduction: consistent inversion implies that any latent-space identifiability argument based on the distribution of  $\mathbf{z}_{1:T}$  carries over to the indirect observation setting via  $\widehat{\mathbf{z}}_{1:T} = g(\mathbf{x}_{1:T})$ .

## B.2. Proof of Theorem 4.6

*Proof of Theorem 4.6.* Consider two parameter instances  $\theta$  and  $\theta'$  in the model class of Theorem 4.6. Assume they induce the same observation law for every  $T$ :

$$P_\theta(\mathbf{x}_{1:T}) = P_{\theta'}(\mathbf{x}_{1:T}) \quad \forall T.$$

We show  $\mathcal{G}_\theta$  and  $\mathcal{G}_{\theta'}$  coincide up to the known equivalences in Assumption 4.4.

Because  $\widehat{\mathbf{z}}_{1:T} = g(\mathbf{x}_{1:T})$  is a measurable function of  $\mathbf{x}_{1:T}$ , equality in distribution of  $\mathbf{x}_{1:T}$  implies equality in distribution of  $\widehat{\mathbf{z}}_{1:T}$ :

$$P_\theta(\widehat{\mathbf{z}}_{1:T}) = P_{\theta'}(\widehat{\mathbf{z}}_{1:T}) \quad \forall T.$$

Let  $\mathbf{z}_{1:T}$  (resp.  $\mathbf{z}'_{1:T}$ ) denote the latent process under  $\theta$  (resp.  $\theta'$ ). By Assumption 4.4,  $d_T(\widehat{\mathbf{z}}, \mathbf{z}) \rightarrow 0$  in probability under  $\theta$ , and  $d_T(\widehat{\mathbf{z}}, \mathbf{z}') \rightarrow 0$  in probability under  $\theta'$ .

Fix any test function  $\varphi \in \mathcal{BL}(1, 1)$ . Then

$$\begin{aligned} \mathbb{E}_\theta[\varphi(\mathbf{z}_{1:T})] - \mathbb{E}_{\theta'}[\varphi(\mathbf{z}'_{1:T})] &= \left( \mathbb{E}_\theta[\varphi(\mathbf{z}_{1:T})] - \mathbb{E}_\theta[\varphi(\widehat{\mathbf{z}}_{1:T})] \right) + \left( \mathbb{E}_\theta[\varphi(\widehat{\mathbf{z}}_{1:T})] - \mathbb{E}_{\theta'}[\varphi(\widehat{\mathbf{z}}_{1:T})] \right) \\ &\quad + \left( \mathbb{E}_{\theta'}[\varphi(\widehat{\mathbf{z}}_{1:T})] - \mathbb{E}_{\theta'}[\varphi(\mathbf{z}'_{1:T})] \right). \end{aligned}$$

The middle term is exactly 0 since  $P_\theta(\widehat{\mathbf{z}}_{1:T}) = P_{\theta'}(\widehat{\mathbf{z}}_{1:T})$ . The first and third terms vanish as  $T \rightarrow \infty$  by Lemma B.1 (applied under  $\theta$  and  $\theta'$ , respectively). Therefore, for every  $\varphi \in \mathcal{BL}(1, 1)$ ,

$$\mathbb{E}_\theta[\varphi(\mathbf{z}_{1:T})] - \mathbb{E}_{\theta'}[\varphi(\mathbf{z}'_{1:T})] \xrightarrow{T \rightarrow \infty} 0.$$

Equivalently, the latent path laws  $P_\theta(\mathbf{z}_{1:T})$  and  $P_{\theta'}(\mathbf{z}'_{1:T})$  become indistinguishable (in the bounded-Lipschitz sense induced by  $d_T$ ) as  $T \rightarrow \infty$ , hence share the same limiting latent distribution (up to the equivalences in Assumption 4.4).

Finally, by Assumption 4.5, within the identifiable nonstationary SEM/SSM class of Huang et al. (2019) (adapted to delayed parents), the delayed graph  $\mathcal{G} = (V, E, \tau)$  is uniquely determined by the limiting latent distribution. Thus  $\mathcal{G}_\theta \equiv \mathcal{G}_{\theta'}$ , proving identifiability from  $P(\mathbf{x}_{1:T})$  as  $T \rightarrow \infty$ .  $\square$

### B.3. Proof of Proposition 4.7

*Proof of Proposition 4.7.* Let  $\widehat{\mathbf{z}}_{1:T} = g(\mathbf{x}_{1:T})$  and  $\widehat{S} = h(\widehat{\mathbf{z}}_{1:T})$ . Assume  $\mathcal{L}$  is a (pseudo-)metric (or any loss satisfying the triangle inequality) on score objects. Then

$$\mathcal{L}(\widehat{S}, S^*) = \mathcal{L}(h(\widehat{\mathbf{z}}_{1:T}), S^*) \leq \mathcal{L}(h(\widehat{\mathbf{z}}_{1:T}), h(\mathbf{z}_{1:T})) + \mathcal{L}(h(\mathbf{z}_{1:T}), S^*).$$

By the assumed Lipschitz property of  $h$ ,

$$\mathcal{L}(h(\widehat{\mathbf{z}}_{1:T}), h(\mathbf{z}_{1:T})) \leq L d_T(\widehat{\mathbf{z}}, \mathbf{z}).$$

Taking expectations yields

$$\mathbb{E}[\mathcal{L}(\widehat{S}, S^*)] \leq \mathbb{E}[\mathcal{L}(h(\mathbf{z}_{1:T}), S^*)] + L \mathbb{E}[d_T(\widehat{\mathbf{z}}, \mathbf{z})].$$

Finally, by Cauchy–Schwarz,

$$\mathbb{E}[d_T(\widehat{\mathbf{z}}, \mathbf{z})] = \mathbb{E}\left[\left(\frac{1}{T} \sum_{t=1}^T \|\widehat{\mathbf{z}}_t - \mathbf{z}_t\|_2^2\right)^{1/2}\right] \leq \left(\mathbb{E}\left[\frac{1}{T} \sum_{t=1}^T \|\widehat{\mathbf{z}}_t - \mathbf{z}_t\|_2^2\right]\right)^{1/2},$$

which gives (4).  $\square$

### B.4. Proof of Corollary 4.8

*Proof of Corollary 4.8.* Assume [Assumption 4.4](#), so  $d_T(\widehat{\mathbf{z}}, \mathbf{z}) = \left(\frac{1}{T} \sum_{t=1}^T \|\widehat{\mathbf{z}}_t - \mathbf{z}_t\|_2^2\right)^{1/2} \xrightarrow[T \rightarrow \infty]{P} 0$ , and assume  $h$  is consistent on the true latent process:  $\mathcal{L}(h(\mathbf{z}_{1:T}), S^*) \xrightarrow[T \rightarrow \infty]{P} 0$ . Using the same triangle-inequality step as in the proof of [Proposition 4.7](#) and then the Lipschitz property,

$$\mathcal{L}(\widehat{S}, S^*) = \mathcal{L}(h(\widehat{\mathbf{z}}_{1:T}), S^*) \leq \mathcal{L}(h(\mathbf{z}_{1:T}), S^*) + L d_T(\widehat{\mathbf{z}}, \mathbf{z}).$$

Both terms on the RHS converge to 0 in probability, hence their sum converges to 0 in probability:  $\mathcal{L}(\widehat{S}, S^*) \xrightarrow[T \rightarrow \infty]{P} 0$ .  $\square$

### B.5. Stability of top- $k$ sparsification

In practice we may form a sparse edge set by retaining the top- $k$  largest-magnitude entries of a score matrix. This post-processing is not Lipschitz in general, but it is stable under a mild separation (margin) condition.

**Top- $k$  operator.** For  $v \in \mathbb{R}^m$ , let  $|v|_{(1)} \geq \dots \geq |v|_{(m)}$  be the order statistics of  $\{|v_1|, \dots, |v_m|\}$ . Define  $\text{TopK}_k(v)$  as the set of indices of the  $k$  largest entries of  $|v|$  (with deterministic tie-breaking). For a matrix  $S \in \mathbb{R}^{p \times p}$ , we apply  $\text{TopK}_k$  to  $\text{vec}(S)$ .

**Lemma B.2** (Top- $k$  support stability under a margin). *Let  $v \in \mathbb{R}^m$  and define the margin  $\Delta := |v|_{(k)} - |v|_{(k+1)}$  (with the convention  $|v|_{(m+1)} := 0$ ). If  $\|\widehat{v} - v\|_\infty < \Delta/2$ , then  $\text{TopK}_k(\widehat{v}) = \text{TopK}_k(v)$ .*

*Proof.* Let  $S = \text{TopK}_k(v)$  and  $S^c$  its complement. For any  $i \in S$  and  $j \in S^c$ , we have  $|v_i| - |v_j| \geq \Delta$ . If  $\|\widehat{v} - v\|_\infty < \Delta/2$ , then  $|\widehat{v}_i| \geq |v_i| - \Delta/2$  and  $|\widehat{v}_j| \leq |v_j| + \Delta/2$ , hence  $|\widehat{v}_i| - |\widehat{v}_j| \geq \Delta - \Delta/2 = \Delta/2 > 0$ , so the ordering separating  $S$  and  $S^c$  is preserved (up to the fixed tie-break rule).  $\square$

**Consequence.** If  $\mathcal{L}(\widehat{S}, S^*) \rightarrow 0$  under a loss that controls  $\|\text{vec}(\widehat{S}) - \text{vec}(S^*)\|_\infty$  (e.g., taking  $\mathcal{L}$  as an  $\ell_\infty$  loss), and if the top- $k$  margin of  $\text{vec}(S^*)$  is bounded away from 0, then the top- $k$  support extracted from  $\widehat{S}$  is consistent.

## C. Algorithm Details

---

**Algorithm 2** INCAMA: physics-aware Inversion + Latent-Space Causal Discovery (in detail)

---

**Require:** Observations  $x_{1:T}$  (EEG or fMRI), modality forward operator  $\mathcal{H}_\psi$ , max delay  $D$ , sparsity ratio  $\rho$

**Require:** Train data (simulation): ground-truth adjacency/delays  $(A^*, \tau^*)$  if available

**Ensure:** Reconstructed latent trajectories  $\hat{z}_{1:T}$  and sparse directed graph  $\hat{G} = (\hat{E}, \hat{\tau})$

```

1: Stage 1: physics-aware inversion (modality-specific)
2: if modality = EEG then
3:   /*  $x_t \approx L_\psi z_t + \epsilon_t$  */
4:   Canonicalize montage:  $x_{1:T} \leftarrow \text{MapToCanonical}(x_{1:T})$ 
5:    $\hat{z}_{1:T} \leftarrow g_\theta^{\text{EEG}}(x_{1:T})$ 
6:   /* DeepSIF-style source imaging */
7:   (physics consistency) enforce  $x_{1:T} \approx L_\psi \hat{z}_{1:T}$  via forward reconstruction loss
8: else
9:   /*  $x_t \approx \sum_{\ell=0}^L h_{\psi,\ell} z_{t-\ell} + \epsilon_t$  */
10:   $(\hat{z}_{1:T}, \hat{h}) \leftarrow g_\theta^{\text{fMRI}}(x_{1:T})$ 
11:  /* ROI-specific HRF deconvolution */
12:  (physics consistency) enforce  $x_{1:T} \approx (\hat{z} * \hat{h})_{1:T}$  via BOLD reconstruction loss
13: end if
14: Stage 2: Latent-space causal discovery
15: for  $i = 1$  to  $R$  do
16:    $h_{i,1:T} \leftarrow \text{Mamba}(\hat{z}_{i,1:T})$ 
17: end for
18: Estimate delay-aware interactions via multi-lag kernels
19:  $\hat{z}_{t+1} \approx \sum_{\ell=1}^D A_\ell \hat{z}_{t-\ell} + \xi_t$ 
20: Multi-scale grouping (short/mid/long):  $\{A_\ell^{(g)}\}_{g \in \mathcal{G}, \ell \in \mathcal{L}_g}$ 
21: Aggregate causal strength:
22:  $\hat{C}_{ij} \leftarrow \sum_{g \in \mathcal{G}} w_g \sum_{\ell \in \mathcal{L}_g} |A_{\ell,ij}^{(g)}|$ 
23: Compute dense graph scores (optional):
24:  $G_{\text{dense}} \leftarrow \text{PairwiseMLP}(\{h_i\}_{i=1}^R)$ 
25: Combine scores:
26:  $G_{\text{comb}} \leftarrow (1 - \alpha)G_{\text{dense}} + \alpha \cdot \text{Scale}(\hat{C})$ 
27: Top- $k$  sparsification
28:  $k \leftarrow \lfloor \rho R^2 \rfloor$ 
29:  $M \leftarrow \text{TopKMask}(|G_{\text{comb}}|, k)$ 
30:  $\hat{G} \leftarrow G_{\text{comb}} \odot M$ 
31: /* optional */  $\hat{\tau}_{ij} \leftarrow \arg \max_{\ell \in \{1, \dots, D\}} |A_{\ell,ij}|$ 
32: End-to-end training (simulation)
33: Minimize  $\mathcal{L}_{\text{total}} = \mathcal{L}_{\text{graph}} + \lambda_{\text{asym}} \mathcal{L}_{\text{asym}} + \lambda_{\text{stab}} \mathcal{L}_{\text{stab}}$ 
34: Update  $\theta$  (and causal parameters) by backpropagation so that causal loss shapes inversion
35: return  $(\hat{z}_{1:T}, \hat{G}, \hat{\tau})$ 

```

---

## D. Implementation Details

We propose **INCAMA**, a unified framework designed to solve the physics-aware inverse problem defined in Section 3. As illustrated in Figure 1, our architecture consists of two coupled modules: (1) a physics-aware Inversion Layer that disentangles latent neural drivers from distorted observations, and (2) a Mamba-based Causal Discovery Model that infers directed connectivity via non-stationary state-space modeling.

### D.1. Stage 1: fMRI HRF Deconvolution

Stage 1 addresses the inverse problem of estimating latent neural activity from observed BOLD signals. Since BOLD signals result from the convolution of neural activity with the hemodynamic response function (HRF), we design a learnable deconvolution framework that jointly estimates ROI-specific HRF parameters and underlying neural activity.

**ROI-Specific HRF Estimation.** Based on neuroimaging evidence that hemodynamic response characteristics vary across brain regions, our model estimates individualized HRF parameters for each ROI. Given a BOLD signal  $x \in \mathbb{R}^{L \times 1}$ , a conditional Mamba encoder extracts temporal features, which are then mapped to six HRF parameters via a linear layer:

- **peak\_delay** (3.0–10.0s): delay to main response peak
- **undershoot\_delay** (10.0–20.0s): delay to undershoot peak
- **peak\_disp, undershoot\_disp** (0.5–2.0): dispersion of each component
- **undershoot\_scale** (0.0–1.0): relative magnitude of undershoot
- **kernel\_duration** (28.0–34.0s): effective HRF kernel length

From the predicted parameters, we generate the HRF kernel  $h(t)$  using a double-gamma function:

$$h(t) = \frac{t^{a_1-1} e^{-t/b_1}}{b_1^{a_1} \Gamma(a_1)} - c \cdot \frac{t^{a_2-1} e^{-t/b_2}}{b_2^{a_2} \Gamma(a_2)}, \quad (14)$$

where  $a_1, b_1$  are shape and scale parameters for the main peak,  $a_2, b_2$  for the undershoot, and  $c$  is the undershoot scale.

**Neural Activity Parameter Generation.** We model neural activity as a sequence of spike events. An attention-based parameter generator predicts spike parameters from BOLD features  $\mathbf{F} \in \mathbb{R}^{L \times H}$  extracted by the conditional Mamba encoder. Using learnable query vectors with multi-head attention, we predict for each spike  $k$ :

- **timing**  $t_k$ : spike occurrence time
- **amplitude**  $a_k$ : spike magnitude
- **width**  $w_k$ : spike width (standard deviation)

The neural activity time series is then generated as a sum of Gaussian pulses:

$$n(t) = \sum_{k=1}^K a_k \cdot \exp\left(-\frac{(t-t_k)^2}{2w_k^2}\right) + \epsilon(t), \quad (15)$$

where  $K$  is the number of spikes and  $\epsilon(t)$  is background noise with  $1/f$  characteristics.

**BOLD Reconstruction.** The estimated neural activity  $\hat{n}(t)$  is convolved with the HRF kernel  $h(t)$  to reconstruct the BOLD signal:

$$\hat{x}(t) = (\hat{n} * h)(t). \quad (16)$$

This is implemented via grouped convolution, applying independent HRFs to each ROI.

**Training Objective.** The Stage 1 loss function consists of two terms:

$$\mathcal{L}_{\text{stage1}} = \lambda_{\text{na}} \cdot \text{MSE}(\hat{n}, n^*) + \lambda_{\text{bold}} \cdot \text{MSE}(\hat{x}, x), \quad (17)$$

where  $n^*$  is the ground-truth neural activity from simulation and  $x$  is the input BOLD signal. The first term ensures accurate neural activity estimation, while the second enforces consistency of the HRF model.

## D.2. Stage 1: EEG Source Localization

Stage 1 addresses the inverse problem of estimating latent ROI-level local field potential (LFP) signals from observed scalp EEG measurements. Since scalp EEG signals result from spatial mixing due to volume conduction, we employ DeepSIF (Deep Learning-based Source Imaging Framework) to perform end-to-end learnable source imaging that directly maps sensor-space EEG to source-space neural activity.

**Architecture.** DeepSIF is based on a one-dimensional convolutional neural network (1D CNN) encoder-decoder architecture. Given scalp EEG signals  $\mathbf{E} \in \mathbb{R}^{B \times S \times T}$  (batch size  $B$ , number of sensors  $S$ , time points  $T$ ), DeepSIF outputs ROI-level LFP signals  $\hat{\mathbf{L}} \in \mathbb{R}^{B \times R \times T}$  (number of ROIs  $R$ ).

Specifically, DeepSIF consists of the following layer structure:

1. **First convolutional layer:** Expands  $S$  channels to 256 channels (kernel size 3, padding 1)
2. **Second convolutional layer:** Reduces 256 channels to 128 channels (kernel size 3, padding 1)
3. **Output projection layer:** Maps 128 channels to  $R$  channels ( $1 \times 1$  convolution)

Each convolutional layer is followed by batch normalization and LeakyReLU activation (negative slope 0.1). DeepSIF processes broadband signals directly without frequency division, corresponding to setting the number of frequency bands  $N = 1$ .

**Loss Function.** The training objective for Stage 1 minimizes two reconstruction losses:

**1. Forward Model Reconstruction Loss.** The predicted ROI LFP  $\hat{\mathbf{L}}$  is reconstructed back to scalp EEG using the leadfield matrix  $\mathbf{H} \in \mathbb{R}^{S \times R}$ , and the difference from the actual scalp EEG  $\mathbf{E}$  is measured:

$$\mathcal{L}_{\text{forward}} = \|\mathbf{E} - \mathbf{H}\hat{\mathbf{L}}\|_1. \quad (18)$$

This loss ensures consistency of predictions through the physical forward model and enables unsupervised learning even when ground-truth supervision is unavailable.

**2. Supervised Loss.** When ground-truth ROI LFP  $\mathbf{L}_{\text{gt}}$  is available, direct comparison with predictions is used for learning:

$$\mathcal{L}_{\text{gt}} = \|\hat{\mathbf{L}} - \mathbf{L}_{\text{gt}}\|_2^2. \quad (19)$$

**3. Adaptive Loss Weights.** We apply a curriculum learning strategy that gradually adjusts the weights of loss components during training. For epoch  $e$  with progress  $p = e/E_{\text{max}}$  (total epochs  $E_{\text{max}}$ ):

- **Stability weight:**  $\lambda_{\text{stab}} = 10^{-3} \times (1 + p)$
- **Structural connectivity weight:**  $\lambda_{\text{sc}} = 0.1 \times (1 + 0.5p)$

Early training focuses on reconstruction, while later stages place greater emphasis on structural consistency.

**Training Procedure.** Stage 1 training is performed with the following settings:

- **Optimizer:** AdamW (learning rate  $5 \times 10^{-4}$ , weight decay  $10^{-5}$ )
- **Learning rate scheduler:** Cosine annealing scheduler
- **Gradient clipping:** Maximum norm 1.0
- **Gradient accumulation:** Accumulated over a specified number of steps before update

Parameters of Stage 2 (causal discovery module) are kept frozen, and only Stage 1 parameters are trained. This enables step-by-step learning of source reconstruction and causal discovery.

**Implementation Details.** DeepSIF is implemented as the `Stage1_DeepSIF` class, which internally contains the `DeepSIF` module. During forward propagation, it takes scalp EEG as input and outputs ROI LFP, expanding the output dimensions to  $(B, R, T, 1)$  for compatibility. Loss computation performs both forward model reconstruction using the leadfield matrix and, when possible, direct comparison with ground-truth values. This design enables DeepSIF to provide a source imaging model that satisfies physical constraints while flexibly learning from data.

### D.3. Stage 2: Latent Causal Dynamics via Mamba

Given ROI-level neural activity recovered from Stage 1, our goal is to estimate directed causal connectivity between brain regions. Stage 2 addresses this through three key innovations: (1) **standard Mamba encoder** for efficient ROI time series representation learning, (2) **multi-scale causal kernel** modeling temporal dynamics across different time scales, and (3) **top- $k$  sparsification** for biologically plausible sparse connectivity structure.

### D.3.1. MAMBA ENCODER

To encode neural activity time series for each ROI, we employ a standard Mamba encoder that is shared across all ROIs. The standard Mamba encoder, based on efficient state-space model implementation, captures long-range temporal dependencies with linear complexity, enabling effective modeling of long time series.

For each ROI  $i \in \{1, \dots, R\}$  with neural activity time series  $x_i \in \mathbb{R}^T$  (where  $T$  is the temporal length), the encoding process proceeds as follows:

1. **Input projection:**  $x_i^{\text{proj}} = \text{Linear}(x_i) \in \mathbb{R}^{T \times H}$  where  $H$  is the hidden dimension

2. **Mamba-based encoding:**

$$h_i = \text{Mamba}(x_i^{\text{proj}}) \in \mathbb{R}^{T \times H} \quad (20)$$

3. **Temporal pooling** (optional):  $e_i = \text{AdaptiveAvgPool1d}(h_i) \in \mathbb{R}^H$  when temporal dimension is not preserved

The standard Mamba encoder, as an efficient implementation of state-space models, captures long-range temporal dependencies with linear complexity. By applying the same encoder to all ROIs, we learn shared temporal patterns while allowing ROI-specific characteristics to be captured in subsequent structure learning stages.

### D.3.2. MULTI-SCALE CAUSAL KERNEL

Neural signal transmission occurs at various time scales due to synaptic delays, axonal conduction velocities, and indirect pathway transmission. To explicitly model these multi-scale temporal dynamics, we introduce a multi-scale VAR-like causal kernel that simultaneously considers short-term, mid-term, and long-term temporal dependencies.

The multi-scale causal dynamics are modeled as:

$$\mathbf{x}_{t+1} = \sum_{g \in \mathcal{G}} \sum_{\ell \in \mathcal{L}_g} \mathbf{A}_\ell^{(g)} \mathbf{x}_{t-\ell} + \boldsymbol{\epsilon}_t \quad (21)$$

where  $\mathcal{G} = \{\text{short, mid, long}\}$  denotes temporal scale groups, each with a corresponding lag set  $\mathcal{L}_g$ . For fMRI data with TR = 2.0 seconds:

- **Short-term:**  $\mathcal{L}_{\text{short}} = \{1, 2\}$  TRs (2–4 seconds) — capturing direct neural connections and immediate causal influences
- **Mid-term:**  $\mathcal{L}_{\text{mid}} = \{3, 4, 5\}$  TRs (6–10 seconds) — modeling intermediate pathway transmission and local network dynamics
- **Long-term:**  $\mathcal{L}_{\text{long}} = \{6, 7, \dots, 10\}$  TRs (12–20 seconds) — capturing indirect pathways, feedback loops, and long-range interactions

Each group  $g$  has learnable kernel matrices  $\mathbf{A}_\ell^{(g)} \in \mathbb{R}^{R \times R}$  for each lag  $\ell \in \mathcal{L}_g$ , where  $A_{\ell,ij}^{(g)}$  represents the causal influence strength from ROI  $i$  to ROI  $j$  at time lag  $\ell$  within scale group  $g$ .

The final causal strength matrix  $\mathbf{C} \in \mathbb{R}^{R \times R}$  is computed as a weighted aggregation across all temporal scales:

$$C_{ij} = \sum_{g \in \mathcal{G}} w_g \sum_{\ell \in \mathcal{L}_g} |A_{\ell,ij}^{(g)}| \quad (22)$$

where  $w_g$  are group-specific weights that can emphasize different temporal scales. The absolute value operation  $|\cdot|$  ensures that causal strength is represented as a positive scalar, aggregating influences across all time lags within each scale group.

**Integration with Dense Graph.** The multi-scale causal kernel is integrated with the dense graph learned from ROI embeddings through a weighted combination:

$$\mathbf{G}_{\text{combined}} = (1 - \alpha) \mathbf{G}_{\text{dense}} + \alpha \mathbf{C}_{\text{scaled}} \quad (23)$$

where  $\mathbf{G}_{\text{dense}}$  is the pairwise MLP output from ROI embeddings,  $\mathbf{C}_{\text{scaled}}$  is the multi-scale causal matrix scaled to match the magnitude of  $\mathbf{G}_{\text{dense}}$ , and  $\alpha = 0.1$  is a small mixing coefficient that allows gradual integration of temporal dynamics.

### D.3.3. TOP- $K$ SPARSIFICATION

Real brain networks are extremely sparse, with empirical estimates suggesting that less than 10–15% of possible connections represent actual causal relationships. Standard  $\ell_1$  regularization or threshold-based sparsification methods suffer from gradient vanishing under extreme sparsity and cannot guarantee exact target sparsity ratios.

We apply a top- $k$  selection mechanism that guarantees exact sparsity while maintaining gradient flow through selected connections. The sparsification process consists of three steps:

**1. Dense Graph Generation.** From ROI embeddings  $\mathbf{E} \in \mathbb{R}^{B \times R \times H}$ , we compute a dense causal graph using pairwise MLP:

$$\mathbf{G}_{\text{dense}} = \text{PairwiseMLP}(\mathbf{E}) \in \mathbb{R}^{B \times R \times R} \quad (24)$$

The dense graph is then passed through a learnable activation function that adapts to dataset statistics:

$$\mathbf{G}_{\text{scaled}} = \text{CouplingActivation}(\mathbf{G}_{\text{dense}}) \quad (25)$$

where Coupling Activation applies dataset-aware scaling to prevent scale collapse and ensures outputs are in a normalized space suitable for training.

**2. Top- $K$  Selection.** For each sample in the batch, we select the top  $k$  strongest connections globally:

$$k = \lfloor \rho \cdot R^2 \rfloor \quad (26)$$

where  $\rho \in [0, 1]$  is the target sparsity ratio (e.g.,  $\rho = 0.1$  for 10% connectivity). The selection mask is constructed as:

$$M_{ij}^{(b)} = \begin{cases} 1 & \text{if } (i, j) \in \text{TopK}(|\mathbf{G}_{\text{scaled}}^{(b)}|, k) \\ 0 & \text{otherwise} \end{cases} \quad (27)$$

where  $\text{TopK}(\cdot, k)$  returns the indices of the  $k$  largest entries by absolute value.

**3. Sparse Graph Generation.** The final sparse causal graph is obtained by element-wise multiplication:

$$\mathbf{G}_{\text{sparse}} = \mathbf{G}_{\text{scaled}} \odot \mathbf{M} \quad (28)$$

This approach ensures: (i) **exact target sparsity ratio**  $\rho$  is maintained, (ii) **gradient flow** is preserved through the selected  $k$  edges, and (iii) **robustness** against overfitting to the overwhelming majority of null connections.

**Dynamic Sparsity Scheduling.** During training, we employ a dynamic sparsity schedule that starts with a relatively dense graph and gradually increases sparsity:

$$\rho(t) = \rho_{\text{start}} - (\rho_{\text{start}} - \rho_{\text{end}}) \cdot \min\left(\frac{t}{T_{\text{schedule}}}, 1\right) \quad (29)$$

where  $\rho_{\text{start}} = 0.35$  (35% connections),  $\rho_{\text{end}} = 0.25$  (25% connections), and  $T_{\text{schedule}} = 50$  epochs. This warmup strategy facilitates easier learning in early training while converging to biologically plausible sparse structures in later stages.

## D.4. Training Objectives

Training causal models on biological neural data is challenging due to extreme sparsity, non-stationarity, and measurement noise. Our objective function combines predictive accuracy with biological constraints:

$$\mathcal{L}_{\text{total}} = \mathcal{L}_{\text{MAE}} + \lambda_{\text{asym}} \mathcal{L}_{\text{asym}} + \lambda_{\text{scale}} \mathcal{L}_{\text{scale}} + \lambda_{\text{stab}} \mathcal{L}_{\text{stab}} \quad (30)$$

**1. Top- $K$  Weighted MAE Loss.** To focus learning on the most informative connections, we adopt a weighted MAE loss over the top- $k$  strongest edges:

$$\mathcal{L}_{\text{MAE}} = \frac{1}{|\Omega_k|} \sum_{(i,j) \in \Omega_k} |A_{ij} - \hat{A}_{ij}| \quad (31)$$

where  $\Omega_k$  denotes indices of the top- $k$  largest entries in the ground-truth adjacency matrix. This acts as a robust estimator that prevents overfitting to the overwhelming majority of null connections.

**2. Asymmetry Loss.** To preserve directionality ( $A \rightarrow B$  vs  $B \rightarrow A$ ), we penalize deviations in the asymmetric component:

$$\mathcal{L}_{\text{asym}} = \|(\hat{\mathbf{A}} - \hat{\mathbf{A}}^\top) - (\mathbf{A}^* - \mathbf{A}^{*\top})\|_1 \quad (32)$$

**3. Scale Loss.** To prevent output distribution collapse, we anchor the predicted statistics to target values:

$$\mathcal{L}_{\text{scale}} = |\mu_{\hat{\mathbf{A}}} - \mu^*| + |\sigma_{\hat{\mathbf{A}}} - \sigma^*| \quad (33)$$

**4. Stability Loss.** To ensure dynamical stability (spectral radius  $< 1$ ), we impose a soft constraint via spectral norm:

$$\mathcal{L}_{\text{stab}} = \max \left( 0, \|\hat{\mathbf{A}}\|_2 - 1 \right)^2 \quad (34)$$

The hyperparameters  $\lambda_{\text{asym}}$ ,  $\lambda_{\text{scale}}$ ,  $\lambda_{\text{stab}}$  control the trade-off between predictive accuracy and biological plausibility. We train the entire pipeline end-to-end, allowing the causal objective to guide earlier stages toward representations most suitable for causal discovery.

## E. Experiment Settings

This section summarizes all hyperparameters used to train **INCAMA** across modalities and stages.

### E.1. fMRI Settings (TVB\_realistic\_nonstationary\_10k)

**Data & preprocessing.** All fMRI stages use `data/TVB_realistic_nonstationary_10k` with BOLD normalization enabled.

**Core architecture and optimization.** Table 5 reports the backbone, dimensionality, and optimization hyperparameters across stages.

Category	Stage 1 (BOLD→Neural)	Stage 2 (Neural→Causal)	Stage 3 (Joint)
Backbone	Mamba	Mamba	Mamba
Hidden size	128	128	128
# ROIs	68	68	68
Causality option	—	<code>sparse_top_k</code>	<code>sparse_top_k</code>
Batch size	16	32	32
Epochs	50	50	50
Learning rate	$1 \times 10^{-4}$	$7.5 \times 10^{-5}$	$1 \times 10^{-3}$
Seed	1	1	1

Table 5. fMRI: core architecture and optimization settings.

**Loss weights and regularization.** Table 6 summarizes the loss weights and regularization coefficients used in each stage.

Loss / regularizer	Stage 1	Stage 2	Stage 3
BOLD reconstruction weight	0.5	—	0.5
Coupling loss weight	—	1.0	3.0
Delay loss weight	—	30.0	30.0
$\lambda_{\text{sparse}}$	—	$1 \times 10^{-6}$	0.01
$\lambda_{\text{stab}}$	—	$5 \times 10^{-3}$	$5 \times 10^{-3}$
$\lambda_{\text{sc}}$	—	0.0	0.0
$\lambda_{\text{asym}}$	—	1.0	1.0
$\lambda_{\text{scale}}$	—	0.0	0.0
$\lambda_{\text{lap}}$	—	$5 \times 10^{-4}$	$5 \times 10^{-4}$
$\lambda_{\text{diversity}}$	—	—	10.0
Diversity target std	—	—	0.05
$\lambda_{\text{scale\_match}}$	—	—	1.0
$\lambda_{\text{recall}}$	—	—	0.1

Table 6. fMRI: loss weights and regularization hyperparameters.

**Stage 2–3 details (selection, schedules, statistics, toggles).** Table 7 reports the remaining hyperparameters that are specific to the causal module and its training schedule.

Table 7. fMRI: Stage 2–3 selection/schedules/statistics and architectural toggles.

Category	Stage 2	Stage 3
<b>Sparsity / selection</b>		
Sparsity ratio	0.15	—
MAE Top-K ratio	0.25	0.35
Edge weight	1.5	1.5
Edge threshold	0.015	0.015
Edge percentile	0.9	0.9
Scale weight	0.1	0.1
<b>Scheduling</b>		
Regularization warmup epochs	3	3
MAE Top-K start ratio	0.15	0.15
MAE Top-K end ratio	0.05	0.05
MAE Top-K schedule length	10 epochs	10 epochs
<b>Coupling statistics</b>		
Auto coupling statistics	Enabled	Enabled
Auto statistics samples	512	512
Coupling norm	1.0	1.0
<b>Architecture toggles</b>		
Multi-scale	Enabled	Enabled
Groups mode	default	default
Laplacian	Enabled	Enabled
Downsample factor	1	1
Efficient GAT	Disabled	Disabled
Preserve temporal	Disabled	Disabled

**Notes (fMRI).** As shown in Table 6, Stage 3 increases the coupling weight (1.0 → 3.0) and sparsity regularization ( $10^{-6} \rightarrow 10^{-2}$ ), and introduces diversity, scale-matching, and recall regularization to stabilize joint training.

## E.2. EEG Settings (nonstationary realistic datasets)

**Data & preprocessing.** EEG stages use `data_10k_nonstationary_realistic`. ENIGMA structural connectivity is enabled.

**Stage-wise core settings.** Table 8 summarizes architecture, training, and checkpointing across EEG stages.

Category	Stage 1 (DeepSIF pretrain)	Stage 2 (Causal mapping)	Stage 5 (Joint finetune)
Architecture	DeepSIF	Mamba	DeepSIF + Causal Mapper (Mamba)
# ROIs	68	68	68
Preserve temporal	—	0	0
ENIGMA SC	Enabled	Enabled	Enabled
Batch size	32	32	16
Epochs	50	50	20
Learning rate	$5 \times 10^{-4}$	$7.5 \times 10^{-5}$	$1 \times 10^{-5}$
Seed	2	2	1
Checkpoints	—	—	Stage 1 + Stage 2 pretrained

Table 8. EEG: stage-wise core settings.

**Stage 2 and Stage 5 details.** Table 9 reports regularization, edge filtering, scheduling, statistics, and architecture toggles for the EEG causal module.

Table 9. EEG: Stage 2 and Stage 5 regularization, edge filtering, schedules, and toggles.

Category	Stage 2	Stage 5
<b>Regularization hyperparameters</b>		
$\lambda_{\text{sparse}}$	$1 \times 10^{-6}$	$1 \times 10^{-6}$
$\lambda_{\text{stab}}$	$5 \times 10^{-3}$	$5 \times 10^{-3}$
$\lambda_{\text{sc}}$	0.0	0.0
$\lambda_{\text{asym}}$	1.0	1.0
$\lambda_{\text{lap}}$	$5 \times 10^{-4}$	$5 \times 10^{-4}$
<b>Edge filtering</b>		
Edge weight	1.5	1.5
Edge threshold	0.015	0.015
Edge percentile	0.9	0.9
Scale weight	0.002	0.002
<b>Scheduling / MAE Top-K</b>		
MAE Top-K start ratio	0.35	0.35
MAE Top-K end ratio	0.25	0.25
MAE Top-K schedule length	50 epochs	20 epochs
Regularization warmup epochs	40	20
<b>Coupling statistics</b>		
Auto coupling statistics	Enabled	Enabled
Auto statistics samples	512	512
<b>Architecture toggles</b>		
Multi-scale	Enabled	Enabled
Groups mode	default	checkpoint_compat
Laplacian	Enabled	Enabled

**Common EEG settings.** WandB logging is enabled; ENIGMA structural connectivity is enabled across EEG stages.

### E.3. Compute / Server Details

The compute environment is summarized in Table 10.

Component	Specification
GPU	7× NVIDIA GeForce RTX 3090
GPU memory	24,576 MiB per GPU ( $\approx$ 24 GB), $\approx$ 168 GB total
Driver / CUDA	Driver 550.90.07; CUDA 12.4 (driver), 12.5 (compiler)
CPU	Intel Xeon Gold 6240R @ 2.40 GHz
Cores / threads	48 cores (24×2 sockets), 96 threads (HT)
Max clock	4.0 GHz
RAM	502 GB total (436 GB available)
Swap	8 GB
OS / Python	Ubuntu 20.04.6 LTS; Python 3.8.10

Table 10. Compute environment used for all experiments.

## F. EEG Simulation Framework: Stationary and Non-stationary Data Generation

This appendix describes the physics-aware EEG simulation framework used to generate stationary and non-stationary datasets with biologically plausible characteristics. The simulator balances biological realism, controllability, and scalability, while providing ground-truth causal topology, time-varying coupling strengths, and transmission delays.

### F.1. At-a-glance summary

Component	Key choices
ROI parcellation	Desikan–Killiany atlas, $N = 68$ ROIs
Structural connectivity	ENIGMA SC (healthy controls; MNI coordinates)
Effective connectivity	SC-to-EC sparsification + directionality + self-inhibition
Stationarity modes	Stationary ( $\sigma_{\text{drift}} = 0$ ) vs. non-stationary AR(1) drift ( $\rho = 0.90$ , $\sigma_{\text{drift}} = 0.10$ )
Delays	Distance-based: $\tau_{ij} = d_{ij}/v + \tau_{\text{syn}}$ , with clipping (5–20 ms)
Neural dynamics	Neural mass with band assignments (alpha-dominant) + synaptic time constants
Forward model	Leadfield $L \in \mathbb{R}^{129 \times N}$ (GSN-128 + Cz) + low-rank perturbation
Sensor-space shaping	Band-weighted reconstruction + correlation control + RMS normalization + optional artifacts
Downsampling	500 Hz $\rightarrow$ 250 Hz via FIR anti-aliasing ( <code>scipy.signal.decimate</code> , factor 2)
Outputs	LFP $X$ , topology $M$ , coupling $B$ or $B_t$ , delays $\tau$ , EEG, leadfield, metadata

Table 11. At-a-glance summary of the EEG simulation framework.

### F.2. Stationary vs. non-stationary coupling dynamics

We generate two EEG dataset variants with identical biological constraints but different coupling dynamics (Table 12).

Property	Stationary	Non-stationary
Coupling matrix	Fixed $B \in \mathbb{R}^{N \times N}$	Time-varying $B_t \in \mathbb{R}^{T \times N \times N}$
Topology mask	Implicit in $B$	Fixed $M \in \{0, 1\}^{N \times N}$
Construction	—	$B_t = M \odot W_t$
Drift process	$\sigma_{\text{drift}} = 0.0$	AR(1): $\rho = 0.90$ , $\sigma_{\text{drift}} = 0.10$

Table 12. Stationary vs. non-stationary dataset generation.

### F.3. Structural connectivity and causal topology

**ENIGMA structural connectivity.** We leverage ENIGMA structural connectivity (SC) under the Desikan–Killiany atlas ( $N = 68$  ROIs), providing biologically grounded connectivity and ROI coordinates in MNI space.

**SC-to-effective connectivity conversion.** Because SC is dense, we convert it to sparse effective connectivity using the procedure summarized in Table 13.

Step	Specification
Weak connection filtering	Remove bottom 50% weakest SC edges
Probabilistic sampling	Retain $(i, j)$ with probability $\min(1, \text{SC}_{\text{norm}}(i, j) \cdot r_{\text{retention}})$ , $r_{\text{retention}} = 1.5$
Target density	10–15% off-diagonal density (effective connectivity)
Directional bias	63% feedforward-only, 30% bidirectional, 7% feedback-only
Self-inhibition	Add self-connection with probability $p_{\text{self}} = 0.25$ per ROI

Table 13. Procedure for converting dense ENIGMA SC into sparse effective connectivity.

### F.4. Distance-based transmission delays

Each directed edge is assigned a transmission delay

$$\tau_{ij} = \frac{d_{ij}}{v} + \tau_{\text{syn}},$$

with parameters summarized in Table 14.

Quantity	Specification
Distance $d_{ij}$	Euclidean distance between ROI centroids (mm; MNI coordinates)
Conduction velocity $v$	$v \sim \mathcal{U}(6.0, 12.0)$ m/s
Synaptic delay $\tau_{\text{syn}}$	$\tau_{\text{syn}} \sim \mathcal{U}(0.001, 0.003)$ s (1–3 ms)
Clipping	Delays clipped to 5–20 ms
Self-delays	Self-connections: 5–10 ms (distance-independent)

Table 14. Delay model and parameter ranges.

## F.5. Neural mass model configuration

**Frequency band assignments.** Each ROI is assigned a dominant band with probability

$$P(\text{band}) = [0.10, 0.15, 0.70, 0.05, 0.0] \text{ for [Delta, Theta, Alpha, Beta, Gamma].}$$

Table 15 summarizes the spectral and synaptic parameters.

Parameter	Specification
Band distribution	Delta 10%, Theta 15%, Alpha 70%, Beta 5%, Gamma 0%
Alpha band	8–13 Hz (dominant in resting-state mimicry)
Excitatory time constant $\tau_E$	$\tau_E \sim \mathcal{U}(0.010, 0.015)$ s (10–15 ms)
Inhibitory time constant $\tau_I$	$\tau_I \sim \mathcal{U}(0.060, 0.100)$ s (60–100 ms)
Sigmoid parameters	threshold = 0.5, slope = 2.0

Table 15. Neural mass model spectral and synaptic parameters.

## F.6. Time-varying coupling weights (non-stationary only)

For non-stationary datasets, coupling weights evolve via AR(1) drift:

$$\delta_t^{(i,j)} = \rho \delta_{t-1}^{(i,j)} + \epsilon_t, \quad w_t^{(i,j)} = w_0^{(i,j)} + \delta_t^{(i,j)}, \quad \epsilon_t \sim \mathcal{N}(0, \sigma_{\text{drift}}^2).$$

Key choices are summarized in Table 16.

Quantity	Specification
AR(1) coefficient	$\rho = 0.90$
Drift noise	$\sigma_{\text{drift}} = 0.10$
Initial weights $w_0^{(i,j)}$	From normalized SC, clipped to [0.03, 0.3]
Sign assignment	Self: inhibitory (negative); inter-ROI: 80% excitatory, 20% inhibitory

Table 16. Non-stationary drift process and coupling initialization.

## F.7. LFP generation

**Latent activity constraints.** LFP generation enforces: (i) delayed coupling via  $\tau$ , (ii) band-specific oscillations per ROI, (iii) slow amplitude modulation (0.1–0.5 Hz), and (iv) signal mixing (30% original, 70% clean oscillation).

## F.8. Leadfield matrix and scalp EEG generation

**Leadfield matrix.** We generate a leadfield  $\mathbf{L} \in \mathbb{R}^{129 \times N}$  using the HydroCel GSN-128 layout (129 channels including Cz reference) with standard 3D electrode coordinates. To model inter-individual variability, we apply a low-rank perturbation (magnitude 0.8–1.5, rank 5–10).

**Scalp projection.** ROI activity  $\mathbf{X}(t)$  is projected to sensor space as

$$\mathbf{y}_{\text{raw}}(t) = \mathbf{X}(t)\mathbf{L}^\top.$$

**Sensor-space shaping.** We match empirical resting-state statistics by combining band-filtered components from  $\mathbf{y}_{\text{raw}}$  with channel-specific synthetic oscillations. The target band mixture and shaping steps are summarized in Table 17.

Table 17. EEG sensor-space shaping: target band mixture, correlation control, normalization, and artifacts.

Component	Specification
Target band mixture	Delta 10%, Theta 12%, <b>Alpha 70%</b> , Beta 6%, Gamma 2%
Band extraction	Extract each band from raw EEG to preserve spatial correlation structure
Synthetic oscillations	Generate independent oscillations per channel (100% channel-specific)
Band weighting	Alpha: raw_weight = 3.0, synth_weight = 2.5; other bands use lower weights
Correlation target	Inter-channel correlation 0.2–0.4
Decorrelation strategy	Add independent $1/f$ noise per channel; minimize shared noise; avoid average reference
RMS normalization	target_RMS $\sim \mathcal{U}(30, 50)$ $\mu\text{V}$ per channel; soft-clip outliers $> 80 \mu\text{V}$ via $\tanh$
Optional artifacts: blinks	10–20/min, duration $\sim 300$ ms, stronger in frontal channels
Optional artifacts: muscle	20–60 Hz, duration 100–500 ms, stronger in temporal/peripheral channels
Optional artifacts: $1/f$	Spectral slope $1/f^{1.2}$ ; 95% shared, 5% independent per channel

## F.9. Downsampling with anti-aliasing

Signals are downsampled using `scipy.signal.decimate` with FIR filtering (Table 18).

Quantity	Specification
Original sampling rate	500 Hz
Downsampling factor	2 (default)
Effective sampling rate	250 Hz
Method	FIR anti-aliasing via <code>scipy.signal.decimate</code>

Table 18. Downsampling configuration.

## F.10. Validation checks

The first subject (`subject_0000`) is automatically validated against biological plausibility checks summarized in Table 19.

Object	Metric	Target range / criterion
EEG	RMS amplitude	10–100 $\mu\text{V}$
EEG	Frequency distribution	Alpha band 30–50% (target: 70%)
EEG	Spatial correlation	0.2–0.5
EEG	Kurtosis	3–8 (artifact-driven)
LFP	Std. deviation	0.2–0.8
LFP	Oscillatory content	Clear frequency bands present
LFP	Connectivity-driven dynamics	Consistent with coupling matrix
Leadfield	Rank	$\geq N_{\text{ROIs}}$
Leadfield	Condition number	Numerical stability check
Topology	Sparsity	10–20% off-diagonal density
Topology	Asymmetry	Directional connections verified
Topology	Hierarchy	Feedforward/feedback ratio enforced

 Table 19. Automatic plausibility validation for `subject_0000`.

## F.11. Output file structure

Each subject directory (`subject_XXXX/`) contains the files listed in Table 20.

## F.12. Summary of biological plausibility constraints

The simulation enforces the biological realism constraints listed in Table 21.

File	Contents (shape)
X.npy	LFP signal ( $T, N$ )
B_t.npy	Time-varying couplings ( $T, N, N$ ) [Non-stationary]
B.npy	Fixed coupling matrix ( $N, N$ ) [Stationary]
M.npy	Fixed topology mask ( $N, N$ )
Tau.npy	Delay matrix ( $N, N$ )
EEG.npy	Scalp EEG signal ( $T, 129$ )
leadfield.npy	Leadfield matrix ( $129, N$ )
channel_names.npy	Channel names (129, )
sensor_positions.npy	Sensor positions (129, 3)
meta.json	Metadata (sampling frequency, duration, parameters, etc.)

Table 20. Per-subject output files produced by the EEG simulator.

Constraint	Implementation
Real brain connectivity	ENIGMA SC (healthy controls)
Distance-based delays	$v \in [6, 12]$ m/s; synaptic delay 1–3 ms; clip 5–20 ms
Spectral realism	Alpha dominance (70%) in ROI band assignments; sensor target mixture uses alpha 70%
Electrode layout	HydroCel GSN-128 + Cz (129 channels)
Spatial correlations	Target inter-channel correlation 0.2–0.4 via noise-based decorrelation
Amplitude realism	RMS $\sim \mathcal{U}(30, 50)$ $\mu$ V with soft clipping
Artifacts	Optional eye blinks + muscle bursts + $1/f$ noise
$1/f$ spectrum	Slope $1/f^{1.2}$ (with shared/independent components)
E/I balance	80% excitatory, 20% inhibitory inter-ROI; self inhibitory
Hierarchy	Feedforward/bidirectional/feedback = 63% / 30% / 7%

Table 21. Key biological plausibility constraints enforced by the simulator.

These design choices ensure the generated EEG preserves key empirical characteristics while providing synthetic data with known causal structure for principled model training and evaluation.

## G. fMRI Simulation Framework: Stationary and Non-stationary Data Generation

This appendix describes the physics-aware fMRI simulation framework used to generate stationary and non-stationary fMRI datasets with biologically plausible characteristics. The simulator is based on The Virtual Brain (TVB) architecture and provides ground truth for causal topology, coupling strengths (fixed or time-varying), conduction delays, and neural activity prior to hemodynamic filtering.

### G.1. At-a-glance summary

Component	Key choices
ROI parcellation	Desikan–Killiany atlas, $N = 68$ ROIs
Structural connectivity	ENIGMA SC (healthy controls; MNI coordinates)
Effective connectivity	SC-to-EC sparsification + directionality + self-inhibition
Stationarity modes	Stationary (fixed $\mathbf{B}$ ) vs. non-stationary AR(1) drift ( $\rho = 0.90$ , $\sigma_{\text{drift}} = 0.10$ )
Delays	Distance-based: $\tau_{ij} = d_{ij}/v + \tau_{\text{syn}}$ , clipped (2.5–50 ms)
Neural dynamics	Wilson–Cowan E/I neural mass model with external drive + delayed coupling
Hemodynamics	ROI-specific HRF (double-gamma), normalized and scaled to 1–5% PSC
Simulation resolution	High-res simulation at 100 Hz ( $dt = 10$ ms) then downsample to TR (e.g. 2.0 s)
BOLD preprocessing	Smoothing, high-pass 0.008 Hz, optional low-pass 0.15 Hz, PSC conversion
Dataset scale	10,000 subjects per condition; duration 480 s; TR 2.0 s; 240 timepoints
Outputs	BOLD, neural activity, $\mathbf{B}$ or $\mathbf{B}_t$ , topology $\mathbf{M}$ , delays $\tau$ , HRF params

Table 22. At-a-glance summary of the fMRI simulation framework.

### G.2. Stationary vs. non-stationary coupling dynamics

We generate stationary and non-stationary fMRI datasets that share the same biological constraints but differ in coupling dynamics (Table 23).

Property	Stationary	Non-stationary
Coupling	Fixed $\mathbf{B} \in \mathbb{R}^{N \times N}$	Time-varying $\mathbf{B}_t \in \mathbb{R}^{T \times N \times N}$
Topology mask	Implicit in $\mathbf{B}$	Fixed $\mathbf{M} \in \{0, 1\}^{N \times N}$
Construction	—	$\mathbf{B}_t = \mathbf{M} \odot \mathbf{W}_t$
Drift process	—	AR(1): $\rho = 0.90$ , $\sigma_{\text{drift}} = 0.10$
Temporal resolution	TR resolution	Generated at 100 Hz, averaged to TR

Table 23. Stationary vs. non-stationary coupling generation.

### G.3. ROI-specific hemodynamic response function (HRF)

**HRF heterogeneity.** We incorporate ROI-specific HRF parameters to reflect regional variability in hemodynamic responses. Each ROI  $i$  is assigned a double-gamma HRF

$$h_i(t) = \frac{t^{a_1^{(i)}-1} e^{-t/b_1^{(i)}}}{b_1^{(i)} a_1^{(i)} \Gamma(a_1^{(i)})} - c^{(i)} \cdot \frac{t^{a_2^{(i)}-1} e^{-t/b_2^{(i)}}}{b_2^{(i)} a_2^{(i)} \Gamma(a_2^{(i)})},$$

where  $(a_1^{(i)}, b_1^{(i)})$  and  $(a_2^{(i)}, b_2^{(i)})$  are derived from peak and undershoot delays, respectively. HRFs are normalized to unit peak and scaled to yield realistic BOLD changes (1–5% PSC).

Key HRF parameter ranges and grouping are summarized in Table 24.

### G.4. Structural connectivity and causal topology

**ENIGMA structural connectivity.** We use ENIGMA structural connectivity (SC) under the Desikan–Killiany atlas ( $N = 68$  ROIs) to ground the topology in biologically realistic anatomy.

Quantity	Specification
Peak delay $t_{\text{peak}}^{(i)}$	[4.0, 9.0] s
Undershoot delay $t_{\text{undershoot}}^{(i)}$	[12.0, 22.0] s
Undershoot scale $c^{(i)}$	[0.15, 0.50]
ROI HRF groups	Fast (peak $\sim$ 5–6 s), Medium (6–7 s), Slow (6.5–8 s)
Normalization / scaling	Unit peak; scaled to 1–5% PSC

Table 24. ROI-specific HRF parameterization (double-gamma).

**SC-to-effective connectivity conversion.** Because SC is dense, we convert it to sparse effective connectivity using the procedure summarized in Table 25.

Step	Specification
Weak connection filtering	Remove bottom 25% weakest SC edges
Probabilistic sampling	Retain $(i, j)$ with probability $\min(1, \text{SC}_{\text{norm}}(i, j) \cdot r_{\text{retention}})$ , $r_{\text{retention}} = 1.5$
Target density	10–15% off-diagonal density
Directional bias	45% feedforward-only, 50% bidirectional, 5% feedback-only
Self-inhibition	Add self-connection with probability $p_{\text{self}} = 0.25$ per ROI

Table 25. Procedure for converting ENIGMA SC into sparse effective connectivity for fMRI.

## G.5. Distance-based conduction delays

Transmission delays are computed from inter-regional distances:

$$\tau_{ij} = \frac{d_{ij}}{v} + \tau_{\text{syn}}.$$

Parameters are summarized in Table 26.

Quantity	Specification
Distance $d_{ij}$	Euclidean distance between ROI centroids (mm; MNI coordinates)
Conduction velocity $v$	$v \sim \mathcal{U}(4.0, 8.0)$ m/s
Synaptic delay $\tau_{\text{syn}}$	$\tau_{\text{syn}} \sim \mathcal{U}(0.003, 0.008)$ s (3–8 ms)
Clipping	2.5–50 ms
Self-delays	3–8 ms (distance-independent)

Table 26. Distance-based conduction delay model.

## G.6. Wilson–Cowan neural mass model

**Local dynamics.** Latent neural activity is generated using a Wilson–Cowan neural mass model with excitatory/inhibitory subpopulations per ROI. Local parameters and time constants are summarized in Table 27.

Quantity	Specification
$w_{EE}^{(i)}$	$\mathcal{U}(1.2, 1.6)$
$w_{EI}^{(i)}$	$\mathcal{U}(0.8, 1.2)$
$w_{IE}^{(i)}$	$\mathcal{U}(1.0, 1.4)$
$w_{II}^{(i)}$	$\mathcal{U}(0.4, 0.8)$
$\tau_E$	0.010 s (10 ms)
$\tau_I$	0.100 s (100 ms)
Activation	$\sigma(x) = 1/(1 + \exp(-2x))$

Table 27. Wilson–Cowan local parameters and time constants.

**Dynamics.** For ROI  $i$ ,

$$\tau_E \dot{E}_i(t) = -E_i(t) + \sigma\left(w_{EE}^{(i)} E_i - w_{EI}^{(i)} I_i + u_i(t)\right), \quad (35)$$

$$\tau_I \dot{I}_i(t) = -I_i(t) + \sigma\left(w_{IE}^{(i)} E_i - w_{II}^{(i)} I_i\right). \quad (36)$$

**External input.** The external drive combines pink noise, infraslow oscillations, and sparse events, with weights summarized in Table 28:

$$u_i^{\text{external}}(t) = 0.5 \text{ slow}_i(t) + 0.3 \text{ pink}_i(t) + 0.2 \text{ events}_i(t).$$

Component	Specification
Pink noise	Independent $1/f$ noise per ROI
Slow fluctuations	0.01–0.04 Hz; sum of 8 sinusoids with random phases
Sparse events	Rate $\sim 0.08/\text{s}$ ; duration $\sim 150 \text{ ms}$
Mixture weights	slow: 0.5, pink: 0.3, events: 0.2

Table 28. External input components for Wilson–Cowan dynamics.

**Delayed coupling input.** Coupled input is

$$u_i^{\text{coupled}}(t) = \sum_{j=1}^N B_{ji}(t) E_j(t - \tau_{ji}), \quad u_i(t) = u_i^{\text{external}}(t) + 0.05 u_i^{\text{coupled}}(t).$$

The coupling term is scaled (0.05) to maintain stability.

### G.7. High-resolution simulation, HRF convolution, and TR downsampling

Neural dynamics are simulated at 100 Hz ( $dt = 0.01 \text{ s}$ ) prior to hemodynamic filtering and TR downsampling. The end-to-end pipeline is summarized in Table 29.

Step	Specification
Simulation	Euler integration with $dt = 0.01 \text{ s}$ at 100 Hz; store $E_i(t)$
Noise / smoothing	Add 2% pink noise; Gaussian smoothing with $\sigma = 0.3 \text{ s}$
Hemodynamics	Convolve each ROI with its HRF kernel $h_i(t)$
TR downsampling	Average over $T_{\text{TR}}/dt$ samples (e.g. TR=2.0 s)

Table 29. High-resolution simulation pipeline prior to TR sampling.

### G.8. Time-varying coupling weights (non-stationary only)

For non-stationary datasets, coupling weights evolve via AR(1) drift at 100 Hz:

$$\delta_t^{(i,j)} = \rho \delta_{t-1}^{(i,j)} + \epsilon_t, \quad w_t^{(i,j)} = w_0^{(i,j)} + \delta_t^{(i,j)}, \quad \epsilon_t \sim \mathcal{N}(0, \sigma_{\text{drift}}^2),$$

with typical values  $\rho = 0.90$  and  $\sigma_{\text{drift}} = 0.10$ . Initialization and constraints are summarized in Table 30.

Quantity	Specification
AR(1) coefficient	$\rho = 0.90$
Drift noise	$\sigma_{\text{drift}} = 0.10$
Initialization	$w_0^{(i,j)} = 0.1 + 1.4 \cdot \frac{\text{SC}_{\text{norm}}(i,j) - \text{SC}_{\text{min}}}{\text{SC}_{\text{max}} - \text{SC}_{\text{min}}}$
Clipping	$w_t^{(i,j)} \in [0.1, 1.5]$ at each timestep
Sign assignment	Self: inhibitory; inter-ROI: 85% excitatory, 15% inhibitory
Downsampling	Average $\mathbf{B}_t$ over each TR window to get TR-resolution $\mathbf{B}_t \in \mathbb{R}^{T \times N \times N}$

Table 30. Non-stationary drift process and coupling constraints (fMRI).

### G.9. BOLD preprocessing and PSC conversion

To match empirical resting-state fMRI characteristics while preserving low-frequency content, we apply the preprocessing steps in Table 31.

This preprocessing targets PSC ranges of roughly  $\pm 3\text{--}8\%$  (std.  $\sim 1.5\text{--}4\%$ ) while preserving the dominant 0.01–0.04 Hz band.

Step	Specification
Temporal smoothing	Gaussian smoothing with $\sigma = 0.5$ TR
High-pass filtering	2nd-order Butterworth, cutoff 0.008 Hz
Low-pass filtering (optional)	2nd-order Butterworth, cutoff 0.15 Hz (below Nyquist for TR=2.0 s)
PSC conversion	Center each ROI; scale to target std. 20.0 (PSC units); ROI amplitude factor $\sim \mathcal{U}(0.8, 1.2)$

Table 31. BOLD preprocessing for realistic PSC-scale resting-state fMRI.

### G.10. Connectivity constraints and sparsity

**E/I balance and sparsity.** Connectivity is constrained to be sparse (10–15% non-zero off-diagonal density). Inter-regional connections are 85% excitatory and 15% inhibitory; self-connections are always inhibitory.

**Distance-dependent connectivity (synthetic option).** When ENIGMA is not used, synthetic edges follow

$$P(i \leftrightarrow j) \propto \exp\left(-\frac{d_{ij}}{\lambda}\right), \quad \lambda = 0.5,$$

with a 2× boost for local connections ( $d_{ij} < 0.3$ ).

### G.11. Dataset generation protocol and outputs

We generate 10,000 simulated subjects for each condition (stationary and non-stationary). Per-subject randomized components and global simulation settings are summarized in Table 32.

Quantity	Specification
Per-subject randomized components	M, ROI HRFs, local WC parameters, delays $\tau$ ; plus drift params for non-stationary
Duration	480 s (8 min)
TR	2.0 s
# timepoints	240
# ROIs	68
Stored outputs	$\mathbf{X}_{\text{BOLD}} \in \mathbb{R}^{68 \times 240}$ ; $\mathbf{X}_{\text{neural}} \in \mathbb{R}^{68 \times 240}$ ; $\mathbf{B}$ or $\mathbf{B}_t \in \mathbb{R}^{240 \times 68 \times 68}$ ; M; $\tau$ ; per-ROI HRF params

Table 32. Dataset protocol and stored outputs (fMRI).

### G.12. Summary of biological plausibility features

The simulator enforces the biological realism constraints summarized in Table 33.

Constraint	Implementation
Real brain connectivity	ENIGMA SC (healthy controls)
Distance-based delays	$v \in [4, 8]$ m/s; synaptic delay 3–8 ms; clip 2.5–50 ms
HRF heterogeneity	ROI-specific double-gamma HRF; $t_{\text{peak}} \in [4, 9]$ s
Resting-state band	External drive emphasizes 0.01–0.04 Hz fluctuations
$1/f$ realism	Pink-noise component in external input; +2% pink noise added post-sim
Wilson–Cowan dynamics	Explicit E/I subpopulations per ROI
E/I balance	Inter-ROI: 85% excitatory, 15% inhibitory; self inhibitory
Temporal non-stationarity	AR(1) drift in coupling weights (non-stationary only)
Empirical-like preprocessing	Smoothing + filtering + PSC scaling with ROI heterogeneity
Hierarchy	Feedforward/bidirectional/feedback = 45% / 50% / 5%

Table 33. Key biological plausibility constraints enforced by the fMRI simulator.

These design choices yield synthetic fMRI datasets that preserve core empirical properties of resting-state BOLD while providing known causal structure and time-varying connectivity for principled evaluation of causal discovery methods under realistic measurement distortions.

## H. Full Baseline Definitions and Hyperparameters

This appendix provides detailed definitions and hyperparameters for all 16 baseline methods used in our comparative evaluation. Baselines are organized into two categories: fMRI baselines (7 methods) and EEG baselines (9 methods).

### H.1. fMRI Baselines

All baseline methods except rDCM follow a two-stage pipeline: (1) **HRF deconvolution**: BOLD signal  $\rightarrow$  neural activity, and (2) **Causality estimation**: neural activity  $\rightarrow$  causal graph.

#### H.1.1. STATISTICAL BASELINES

**FIR-VAR.** This method combines FIR (Finite Impulse Response) deconvolution with a VAR (Vector AutoRegressive) model. The HRF deconvolution uses a canonical double-gamma HRF kernel (SPM-style) with peak response parameters  $a_1 = 6$ ,  $b_1 = 1$ , undershoot parameters  $a_2 = 16$ ,  $b_2 = 1$ , and undershoot ratio  $c = 1/6$ . The HRF length is 32 timepoints, TR is 2.0 seconds, and Wiener filtering (noise=0.1) is applied for noise robustness. The VAR model uses maximum lag  $p = 2$  (reduced from default 5 to avoid fitting errors), AIC for model selection, coupling strength computed as the sum of absolute coefficients across all lags, and delay estimated as the lag with maximum coefficient. Hyperparameters: sequence length 240, TR 2.0, HRF length 32, max\_lag 2, output normalization enabled with scale 1.2.

**FIR-Granger.** This method combines FIR deconvolution with Granger Causality testing. The HRF deconvolution is identical to FIR-VAR. The Granger causality estimation performs pairwise Granger causality tests with maximum lag 2, significance level 0.05, F-test (SSR F-test), coupling strength set to F-statistic (normalized to [0, 1] range), and delay estimated as the lag with maximum F-statistic. Hyperparameters: same as FIR-VAR, with additional significance parameter 0.05.

**Wiener-VAR.** This method combines Wiener deconvolution with VAR modeling. The Wiener deconvolution operates in the frequency domain using a regularized inverse filter:  $W(f) = H^*(f)/(|H(f)|^2 + \sigma_n^2)$ , where  $H(f)$  is the HRF frequency response and  $\sigma_n^2 = 0.1$  is the estimated noise power. The HRF kernel uses the same canonical double-gamma parameters as FIR. The VAR estimation is identical to FIR-VAR. Hyperparameters: sequence length 240, TR 2.0, HRF length 32, noise\_power 0.1, max\_lag 2, output normalization enabled with scale 1.2.

**Wiener-Granger.** This method combines Wiener deconvolution with Granger Causality. The HRF deconvolution is identical to Wiener-VAR, and the causality estimation is identical to FIR-Granger. Hyperparameters: sequence length 240, TR 2.0, HRF length 32, noise\_power 0.1, max\_lag 2, significance 0.05, output normalization enabled with scale 1.2.

**rDCM.** Regression Dynamic Causal Modeling (rDCM) (Frässle et al., 2021) uses Bayesian inverse inference to directly estimate causal connections from fMRI data without explicit HRF deconvolution. The method employs the TAPAS (Toolbox for Advanced Parameter Averaging) rDCM framework with resting-state model type. Bayesian model inversion is performed with sparsity constraints. Hyperparameters: SNR 3, TR (y\_dt) 2.0 seconds, prior probability (p0\_all) 0.15 (initial sparsity for all connections), iterations 100, filter strength 5, restrictInputs 0, u\_shift 0, type 'r' (resting-state), padding 0, visualization disabled, signal computation enabled. The method does not require training and is evaluated directly as a statistical Bayesian approach.

#### H.1.2. DEEP LEARNING BASELINES

**DeepDeconvTCDF (Option 1).** This end-to-end deep learning method combines LSTM-based deconvolution with the Temporal Causal Discovery Framework (TCDF) (Nadéau & Bengio, 2018). The architecture consists of: (1) **LSTM deconvolution module**: bidirectional LSTM with input size  $R$  (number of ROIs), hidden size 64, 2 layers, outputting neural activity  $(B, R, T)$  with Softplus activation for non-negativity; (2) **TCDF module**: dilated depthwise separable 1D-CNN with kernel size 4, 2 layers, dilation coefficients [1, 4], hidden size 64, processing neural activity to extract causal features; (3) **Feature extraction and graph prediction**: adaptive average pooling for temporal aggregation, 2-layer MLP feature extractor ( $1 \rightarrow 64 \rightarrow 64$ ), pairwise predictor ( $128 \rightarrow 64 \rightarrow 1$ ) for coupling, delay predictor with identical structure, and CouplingActivation for output range  $[-1.2, 1.2]$ . Hyperparameters: n\_rois 48 or 68, tcdf\_kernel 4, tcdf\_layers 2, hidden\_dim 64, lstm\_hidden\_size 64, lstm\_num\_layers 2, batch\_size 32, learning\_rate 1e-3, weight\_decay 1e-5, epochs 50,

loss\_weight\_delay 1.0. Loss functions: MSE for deconvolution (neural activity prediction), MSE for coupling, MSE for delay (only on GT edges).

**EndToEndCNN (Option 2).** This end-to-end 1D-CNN method directly predicts causal graphs from BOLD signals. The architecture consists of: (1) **1D-CNN encoder**: three Conv1d layers ( $R \rightarrow 128 \rightarrow 256 \rightarrow 256$ ) with kernel size 3, padding 1, BatchNorm and LeakyReLU(0.1) after each layer; (2) **Temporal pooling**: adaptive average pooling to  $(B, 256)$ ; (3) **Graph generator**: 3-layer MLP  $(256 \rightarrow 512 \rightarrow 1024 \rightarrow R^2)$  with Dropout(0.1) and LeakyReLU(0.1), outputting  $(B, R, R)$  with CouplingActivation; (4) **Delay head**: 2-layer MLP  $(256 \rightarrow 512 \rightarrow R^2)$  with Dropout(0.1) and LeakyReLU(0.1), outputting  $(B, R, R)$  with Softplus activation (non-negative). Hyperparameters: n\_rois 48 or 68, hidden\_dim 128, intermediate\_dim 512 (hidden\_dim  $\times$  4), dropout 0.1, leaky\_relu\_negative\_slope 0.1, batch\_size 32, learning\_rate 1e-3, weight\_decay 1e-5, epochs 50, loss\_weight\_delay 1.0. Loss functions: MSE for coupling, MSE for delay (only on GT edges).

## H.2. EEG Baselines

All EEG baseline methods follow a two-stage pipeline: (1) **Source localization**: scalp EEG  $\rightarrow$  ROI neural activity, and (2) **Causality estimation**: ROI neural activity  $\rightarrow$  causal graph.

### H.2.1. STATISTICAL BASELINES

**MNE+Granger.** This method combines MNE (Minimum Norm Estimate) (Hämäläinen & Ilmoniemi, 1994) source localization with Granger Causality. MNE uses regularization parameter  $\lambda = 0.1$  and inverse operator  $W = L^T(LL^T + \lambda I)^{-1}$ , where  $L$  is the leadfield matrix. Input is scalp EEG  $(S, T)$  with  $S = 129$  channels and  $T = 2500$  timepoints, output is ROI neural activity  $(R, T)$  with  $R = 68$  ROIs. Granger causality performs pairwise tests with maximum lag (order) 5, Ridge regression regularization  $\alpha = 1e - 3$ , coupling strength computed as  $\log(\text{RSS}_{\text{restricted}}/\text{RSS}_{\text{full}})$ , and delay estimated as the lag with maximum coefficient. Hyperparameters: lambda\_reg 0.1, order 5, alpha 1e-3, sampling frequency 250.0 Hz.

**MNE+VAR.** This method combines MNE source localization with VAR modeling. Source localization is identical to MNE+Granger. VAR estimation uses maximum lag (order) 5, Ridge regression regularization  $\alpha = 1e - 3$ , coupling strength as the sum of absolute coefficients across all lags, and delay as the lag with maximum coefficient. Hyperparameters: lambda\_reg 0.1, order 5, alpha 1e-3, sampling frequency 250.0 Hz.

**sLORETA+Granger.** This method combines sLORETA (standardized Low Resolution Electromagnetic Tomography) (Pascual-Marqui, 2002) source localization with Granger Causality. sLORETA uses regularization parameter  $\lambda = 0.05$  and inverse operator  $W = S^{-1}L^T T$  (including standardization matrix). Input and output dimensions are the same as MNE. Causality estimation is identical to MNE+Granger. Hyperparameters: lambda\_reg 0.05, order 5, alpha 1e-3, sampling frequency 250.0 Hz.

**sLORETA+VAR.** This method combines sLORETA source localization with VAR modeling. Source localization is identical to sLORETA+Granger, and causality estimation is identical to MNE+VAR. Hyperparameters: lambda\_reg 0.05, order 5, alpha 1e-3, sampling frequency 250.0 Hz.

**DeepSIF+Granger.** This method combines DeepSIF (Deep Neural Source Imaging) (Sun et al., 2022) source localization with a Granger Estimator. DeepSIF is a deep learning-based source imaging method with focal constraints, trained end-to-end. Input is scalp EEG  $(B, S, T)$  with  $S = 129$ , output is ROI neural activity  $(B, R, T)$  with  $R = 68$ . The Granger Estimator is a lag-based non-trainable statistical method with maximum lag 10, operating on ROI neural activity to output coupling matrix  $(B, R, R)$  and delay matrix  $(B, R, R)$ . Hyperparameters: n\_sensors 129, n\_sources 68, max\_lag 10, sampling frequency 250.0 Hz, batch\_size 32, learning\_rate 1e-3, epochs 50, self\_threshold 0.1. Loss functions: MSE for source localization (neural activity prediction), BCEWithLogitsLoss for coupling, MSE for delay. Note: Only the source localization stage is trainable; the Granger Estimator has no learnable parameters.

### H.2.2. DEEP LEARNING BASELINES

**DeepSIF+TCN+SparseMLP.** This method combines DeepSIF source localization, a TCN (Temporal Convolutional Network) (Bai et al., 2018) encoder, and a SparseMLP structure learner. DeepSIF architecture and hyperparameters are as described in DeepSIF+Granger. The TCN encoder processes  $(B, R, T)$  input with hidden dimension 64, outputting ROI

embeddings  $(B, R, H)$ . The SparseMLP structure learner takes ROI embeddings and outputs coupling matrix  $(B, R, R)$  and delay matrix  $(B, R, R)$  using BCEWithLogitsLoss for coupling and MSE for delay. Hyperparameters: n\_sensors 129, n\_sources 68, hidden\_dim 64, batch\_size 32, learning\_rate 1e-3, epochs 50, self\_threshold 0.1.

**DeepSIF+GNN+SparseMLP.** This method combines DeepSIF source localization, a GNN (Graph Neural Network) (Kipf & Welling, 2017) encoder, and a SparseMLP structure learner. Source localization is identical to DeepSIF+TCN+SparseMLP. The GNN encoder processes  $(B, R, T)$  input with hidden dimension 64, outputting ROI embeddings  $(B, R, H)$ . The SparseMLP structure learner is identical to DeepSIF+TCN+SparseMLP. Hyperparameters are identical to DeepSIF+TCN+SparseMLP.

**sLORETA+TCN+SparseMLP.** This method combines sLORETA source localization, a TCN encoder, and a SparseMLP structure learner. sLORETA uses the same parameters as described in sLORETA+Granger and is non-trainable (fixed). Causality estimation is identical to DeepSIF+TCN+SparseMLP. Hyperparameters are identical to DeepSIF+TCN+SparseMLP.

**sLORETA+GNN+SparseMLP.** This method combines sLORETA source localization, a GNN encoder, and a SparseMLP structure learner. Source localization is identical to sLORETA+TCN+SparseMLP, and causality estimation is identical to DeepSIF+GNN+SparseMLP. Hyperparameters are identical to DeepSIF+TCN+SparseMLP.

### H.3. Common Evaluation Settings

All baseline methods use the following common evaluation settings: data split 80% train / 10% validation / 10% test, triple repetition which have different random seeds, evaluation metrics including F1 Score, SHD (Structural Hamming Distance), dSHD (directional Structural Hamming Distance), and Directionality Accuracy. Thresholds: self-connection threshold 0.1, edge threshold 0.01 (for F1 calculation). All statistical baseline methods require no training and are evaluated directly. Deep learning baseline methods are trained using the Adam optimizer. Statistical methods normalize outputs to range  $[-1.2, 1.2]$  via the `normalize_coupling_output` function to facilitate comparison with deep learning models.

## I. Metrics

This section provides detailed descriptions of the evaluation metrics used in this paper.

### I.1. F1 Score

F1 Score evaluates the accuracy of edge existence in the predicted causal graph and is computed as the harmonic mean of Precision and Recall:

$$F1 = \frac{2 \cdot \text{Precision} \cdot \text{Recall}}{\text{Precision} + \text{Recall}}, \quad (37)$$

where Precision and Recall are defined as:

$$\text{Precision} = \frac{\text{TP}}{\text{TP} + \text{FP}}, \quad (38)$$

$$\text{Recall} = \frac{\text{TP}}{\text{TP} + \text{FN}}. \quad (39)$$

Here, TP (True Positive) denotes edges that exist in both prediction and ground truth, FP (False Positive) denotes edges that exist only in the prediction, and FN (False Negative) denotes edges that exist only in the ground truth. The predicted continuous coupling strength matrix is binarized using a threshold before evaluation. F1 Score ranges from 0 to 1, with values closer to 1 indicating better alignment between the predicted and true graph structures.

### I.2. Normalized SHD (Structural Hamming Distance)

Normalized SHD measures the discrepancy between two directed graphs in terms of local edge structure, counting edge additions, deletions, and direction reversals.

Let  $A_{\text{pred}}, A_{\text{GT}} \in \{0, 1\}^{N \times N}$  denote the predicted and ground-truth adjacency matrices, with self-loops excluded. The

Structural Hamming Distance (SHD) is defined as

$$\text{SHD} = \text{FP} + \text{FN} + \text{Reverse}, \quad (40)$$

where FP denotes false positive edges ( $A_{\text{pred}}(i, j) = 1, A_{\text{GT}}(i, j) = 0$ ), FN denotes false negative edges ( $A_{\text{pred}}(i, j) = 0, A_{\text{GT}}(i, j) = 1$ ), and Reverse denotes incorrectly oriented edges, defined as unordered node pairs  $\{i, j\}$  for which  $A_{\text{pred}}(i, j) = 1$  and  $A_{\text{GT}}(j, i) = 1$ . Each reversed edge is counted once, not twice.

The normalized SHD is obtained by dividing by the number of possible directed edges:

$$\text{Normalized SHD} = \frac{\text{SHD}}{N(N-1)}. \quad (41)$$

Normalized SHD ranges from 0 to 1, with lower values indicating closer agreement between the predicted and ground-truth graph structures.

### I.3. Normalized dSHD (Direction-aware Structural Hamming Distance)

Normalized dSHD measures the discrepancy between two directed graphs by penalizing missing, spurious, and incorrectly oriented edges, with higher weight assigned to edge reversals.

Let  $G_{\text{pred}}$  and  $G_{\text{GT}}$  denote the predicted and ground-truth graphs with adjacency matrices  $A_{\text{pred}}, A_{\text{GT}} \in \{0, 1\}^{N \times N}$ . Self-loops are excluded. The direction-aware Structural Hamming Distance (dSHD) is defined as

$$\text{dSHD} = |\mathcal{E}_{\text{pred}} \setminus \mathcal{E}_{\text{GT}}| + |\mathcal{E}_{\text{GT}} \setminus \mathcal{E}_{\text{pred}}| + 2 \cdot |\mathcal{R}|, \quad (42)$$

where  $\mathcal{E}_{\text{pred}}$  and  $\mathcal{E}_{\text{GT}}$  are the directed edge sets of the predicted and ground-truth graphs, respectively, and  $\mathcal{R}$  denotes the set of reversed edges, defined as

$$\mathcal{R} = \{(i, j) \mid A_{\text{pred}}(i, j) = 1, A_{\text{GT}}(j, i) = 1, A_{\text{GT}}(i, j) = 0\}, \quad (43)$$

with each unordered node pair counted once. Thus, extra and missing edges are penalized with unit cost, while edge reversals incur a cost of 2, reflecting their greater impact on causal interpretation.

The normalized dSHD is obtained by dividing by the number of possible directed edges:

$$\text{Normalized dSHD} = \frac{\text{dSHD}}{N(N-1)}. \quad (44)$$

Normalized dSHD ranges from 0 to 1, with lower values indicating closer agreement between the inferred and ground-truth causal structures. Unlike intervention-based metrics such as Structural Intervention Distance (SID), dSHD evaluates discrepancies in local causal structure while explicitly penalizing edge orientation errors more heavily.